

✓m (2)

# NAVAL POSTGRADUATE SCHOOL

## Monterey, California

AD-A241 893



## THESIS

MEASUREMENT OF ELECTRON BEAM EMITTANCE  
USING OPTICAL TRANSITION RADIATION AND  
DEVELOPMENT OF A DIFFUSE SCREEN ELECTRON  
BEAM MONITOR

by

Carlton Barrow Reid, Jr.

December 1990

Thesis Advisor:

X.K. Maruyama

Approved for public release; distribution is unlimited

91-14269



91 10 28 042

UNCLASSIFIED

SECURITY CLASSIFICATION OF THIS PAGE

REPORT DOCUMENTATION PAGE				Form Approved OMB No. 0704-0188	
1a REPORT SECURITY CLASSIFICATION <b>UNCLASSIFIED</b>			1b RESTRICTIVE MARKINGS		
2a SECURITY CLASSIFICATION AUTHORITY			3 DISTRIBUTION / AVAILABILITY OF REPORT Approved for public release; distribution is unlimited		
2b DECLASSIFICATION / DOWNGRADING SCHEDULE					
4. PERFORMING ORGANIZATION REPORT NUMBER(S)			5. MONITORING ORGANIZATION REPORT NUMBER(S)		
6a. NAME OF PERFORMING ORGANIZATION <b>Naval Postgraduate School</b>		6b. OFFICE SYMBOL (If applicable) <b>PH</b>	7a. NAME OF MONITORING ORGANIZATION <b>Naval Postgraduate School</b>		
6c. ADDRESS (City, State, and ZIP Code) <b>Monterey, CA 93943-5000</b>			7b. ADDRESS (City, State, and ZIP Code) <b>Monterey, CA 93943-5000</b>		
8a. NAME OF FUNDING / SPONSORING ORGANIZATION		8b. OFFICE SYMBOL (If applicable)	9 PROCUREMENT INSTRUMENT IDENTIFICATION NUMBER		
8c. ADDRESS (City, State, and ZIP Code)			10 SOURCE OF FUNDING NUMBERS		
			PROGRAM ELEMENT NO	PROJECT NO.	TASK NO
			WORK UNIT ACCESSION NO		
11. TITLE (Include Security Classification) <b>MEASUREMENT OF ELECTRON BEAM EMITTANCE USING OPTICAL TRANSITION RADIATION AND DEVELOPMENT OF A DIFFUSE SCREEN ELECTRON BEAM MONITOR</b>					
12. PERSONAL AUTHOR(S) <b>REID, Carlton Barrow, Jr.</b>					
13a TYPE OF REPORT <b>Master's Thesis</b>		13b. TIME COVERED FROM _____ TO _____		14. DATE OF REPORT (Year, Month, Day) <b>1990 December</b>	
15 PAGE COUNT <b>119</b>					
16 SUPPLEMENTARY NOTATION The views expressed in this thesis are those of the author and do not reflect the official policy or position of the Department of Defense and the US Government.					
17 COSATI CODES			18. SUBJECT TERMS (Continue on reverse if necessary and identify by block number)		
FIELD	GROUP	SUB-GROUP	transition radiation; Lorentz Factor;		
			diffraction pattern; charged particle beam		
			profiling		
19 ABSTRACT (Continue on reverse if necessary and identify by block number)					
<p>An experimental technique for measuring electron beam emittance using Optical Transition Radiation (OTR) with the Wartski Interferometer Method has been applied to the Naval Postgraduate School linear electron accelerator. Data for obtaining the emittance of the NPS linac has been collected. A chronology of the procedure for using OTR as a beam diagnostic at the NPS Linac is described in detail.</p> <p>A novel OTR beam monitor consisting of a surface purposely made diffuse was also developed and proved to be an excellent profile monitor. It can be used to measure the shape of the electron beam incident on a vacuum/metal interface over a viewing angle range of +/-1 degrees. Beam current and profile measurements using the diffuse screen were compared with measurements using a front surface mirror and a fluorescent screen. The</p>					
20 DISTRIBUTION / AVAILABILITY OF ABSTRACT <input checked="" type="checkbox"/> UNCLASSIFIED/UNLIMITED <input type="checkbox"/> SAME AS RPT <input type="checkbox"/> DTIC USERS			21. ABSTRACT SECURITY CLASSIFICATION <b>UNCLASSIFIED</b>		
22a NAME OF RESPONSIBLE INDIVIDUAL <b>MARUYAMA, X.K.</b>			22b TELEPHONE (Include Area Code) <b>408-646-2431</b>		22c OFFICE SYMBOL <b>PH/Mx</b>

DD Form 1473, JUN 86

Previous editions are obsolete.

SECURITY CLASSIFICATION OF THIS PAGE

S/N 0102-LF-014-6603

UNCLASSIFIED

UNCLASSIFIED

SECURITY CLASSIFICATION OF THIS PAGE

19. cont.

diffuse screen demonstrated a linear response to current while the fluorescent screen showed an exponential response. The OTR produced the beam incident on the diffuse screen and accurately reflected the shape of the electron beam while the secondary electron effects of the fluorescent screen distorted the image.

Approved for public release; distribution is unlimited

Measurement of Electron Beam Emittance Using Optical  
Transition Radiation and Development of a  
Diffuse Screen Electron Beam Monitor

by

Carlton B. Reid, Jr.  
Captain, United States Army  
B.S., United States Military Academy, 1981


Submitted in partial fulfillment of the  
requirements for the degree of

MASTER OF SCIENCE IN PHYSICS

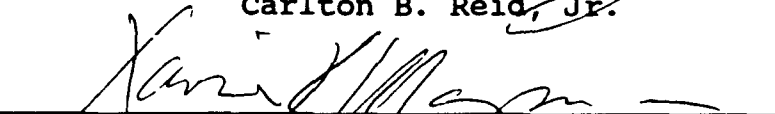
from the

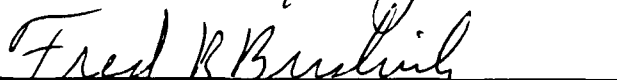
NAVAL POSTGRADUATE SCHOOL  
December 1990

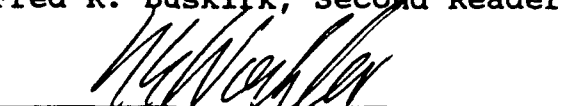
Author:

  
Carlton B. Reid, Jr.

Approved by:

  
Xavier K. Maruyama, Thesis Advisor

  
Fred R. Buskirk, Second Reader

  
Karlheinz E. Woehler, Chairman  
Department of Physics



## ABSTRACT

An experimental technique for measuring electron beam emittance using Optical Transition Radiation (OTR) with the Wartski Interferometer Method has been applied to the Naval Postgraduate School linear electron accelerator. Data for obtaining the emittance of the NPS linac has been collected. A chronology of the procedure for using OTR as a beam diagnostic at the NPS Linac is described in detail.

A novel OTR beam monitor consisting of a surface purposely made diffuse was also developed and proved to be an excellent profile monitor. It can be used to measure the shape of the electron beam incident on a vacuum/metal interface over a viewing angle range of  $\pm 30$  degrees. Beam current and profile measurements using the diffuse screen were compared with measurements using a front surface mirror and a fluorescent screen. The diffuse screen demonstrated a linear response to current while the fluorescent screen showed an exponential response. The OTR produced the beam incident on the diffuse screen and accurately reflected the shape of the electron beam while the secondary electron effects of the fluorescent screen distorted the image.

## TABLE OF CONTENTS

I.	INTRODUCTION.....	1
	A. THEORY OF OPTICAL TRANSITION RADIATION...	1
	B. PURPOSE OF THE EXPERIMENT.....	6
II.	THE EMITTANCE MEASUREMENT.....	8
	A. EXPERIMENTAL SETUP.....	15
	B. THE EMITTANCE MEASUREMENT EXPERIMENT.....	26
III.	THE PROFILE MONITOR EXPERIMENT.....	50
	A. THE DIFFUSE SCREEN EXPERIMENTAL SETUP....	52
	B. COMPUTER SOFTWARE.....	54
	C. DIFFUSE SCREEN EXPERIMENTAL PROCEDURE....	65
IV.	PROFILE MONITOR DATA AND RESULTS.....	71
	A. ANGULAR DEPENDENCE.....	72
	B. CURRENT DEPENDENCE.....	79
V.	CONCLUSIONS.....	102
	A. EMITTANCE MEASUREMENT EXPERIMENT.....	102
	B. BEAM MONITOR EXPERIMENT.....	103
	C. SUGGESTIONS FOR FOLLOW-ON RESEARCH.....	105
	APPENDIX EQUIPMENT LISTING.....	106
	REFERENCES.....	110
	INITIAL DISTRIBUTION LIST.....	111

## I. INTRODUCTION

### A. THEORY OF OPTICAL TRANSITION RADIATION

Transition radiation, TR, is the radiation produced when a particle moves from one medium to another with a different dielectric property. Transition radiation is electromagnetic and produces photons with frequencies which range from the microwave to xray portions of the electromagnetic spectrum (see Figure 1). Optical Transition Radiation, OTR, is defined as that radiation produced in the visible or optical region of the spectrum. Transition radiation was discovered in 1946 after the discovery of Cerenkov radiation. In contrast to transition radiation, Cerenkov radiation is the radiation produced by a charged particle traveling relativistically through a medium and was discovered in 1939 [Ref. 1].

Transition radiation can be explained by the use of Maxwell's inhomogeneous equations and the concept of image charges [Ref. 2]. As the charged particle moves towards a boundary from one side, there is an 'image' charge moving towards the interface from the opposite side and direction (see Figure 2). When the charges meet at the boundary, radiation fields are produced which satisfy Maxwell's inhomogeneous equations. These fields are known as

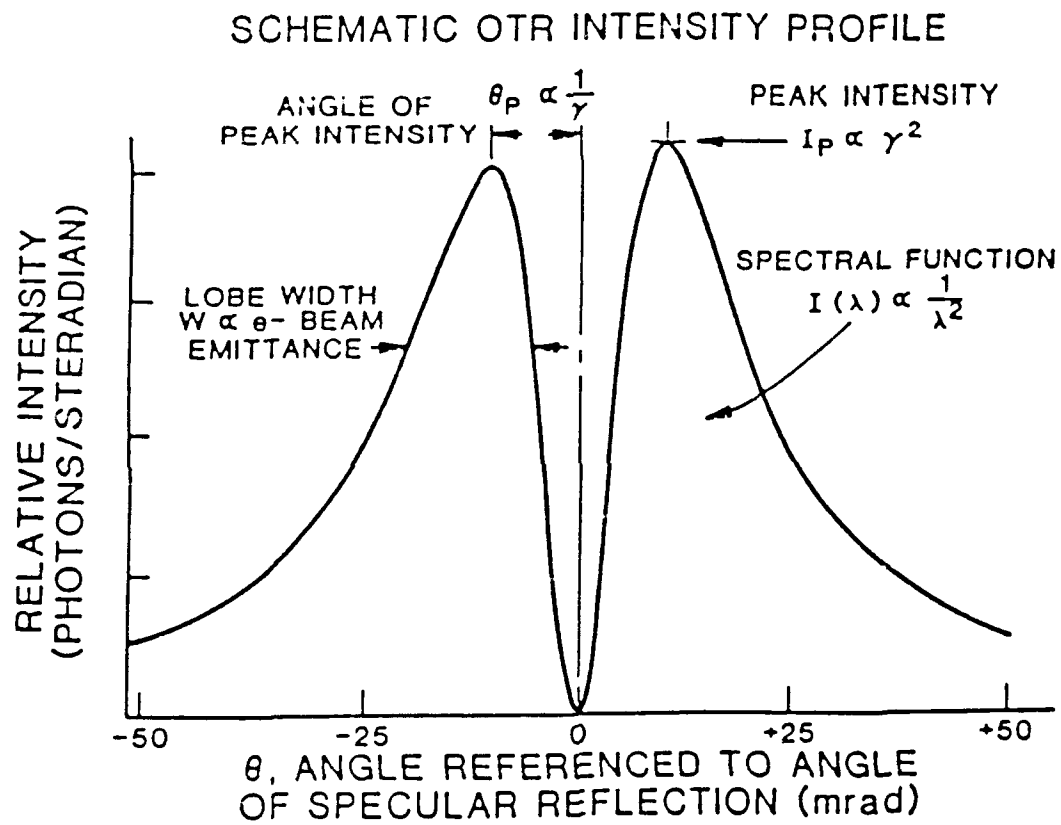


Figure 1: Schematic of the Cone Shaped OTR Intensity Profile. The angle of peak intensity is proportional to the Lorentz factor [Ref. 1].



transition radiation. Ginsburg and Frank developed rigorous mathematical equations to describe the intensity of the radiation per frequency interval per solid angle around the particle's line of motion as a function of the particle's velocity, the dielectric constants of the two media and the angle of observation [Ref. 1],

$$\frac{dI(w, \theta)}{dw d\Omega} = \frac{e^2 \beta^2 \sin^2 \theta}{\pi^2 c [1 - \beta^2 \cos^2 \theta]^2} \quad (1)$$

Equation 1 gives the intensity for a charged particle traveling from a perfect vacuum into a perfectly conducting medium.  $\beta$  is equal to the particle's velocity divided by the speed of light in vacuum.  $\theta$  is the angle of observation (measured from the normal to the surface) about which the solid angle is measured. Thus, equation 1 clearly shows the strong dependence on the angle of observation of the cone shaped radiation pattern.

Transition radiation was shown by Wartschi to possess a number of properties which make it useful in beam diagnostics [Ref. 2]. The principle advantage is its strong dependence on the energy of the particle producing it. It is also polarized with the electric vector lying in the plane defined by the normal to the direction of observation. The peak intensity of the radiation occurs at the angle corresponding to the inverse of the Lorentz factor (Equation

2). The Lorentz factor is equal to the total energy divided by the rest mass energy [Ref 3].

$$\theta_p = \gamma^{-1} = \frac{E}{mc^2} \quad (2)$$

When transition radiation is produced, it is observed in both the forward and backward directions of the interface. The forward transition radiation continues in the same direction as the particle and is difficult to separate from bremsstrahlung radiation. For this experiment, the radiation cone also needed to be captured without exposing the equipment to the electron beam. By turning the interface of the two media 45 degrees, backward transition radiation could be seen 90 degrees from the electron beam separating it from bremsstrahlung radiation and the electron beam. Figure 3 shows the transition radiation patterns for both cases in which the interface is seen at normal incidence and at oblique incidence [Ref 2]. The angle represents the 45 degree oblique angle measured from the electron beamline to the target.

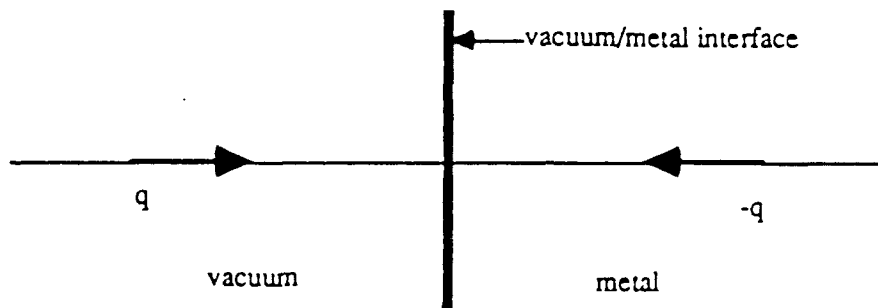


Figure 2: Model of particle and its image particle approaching a vacuum/metal interface thereby acting as a collapsing dipole and producing transition radiation [Ref.2].

#### OPTICAL TRANSITION RADIATION PATTERNS

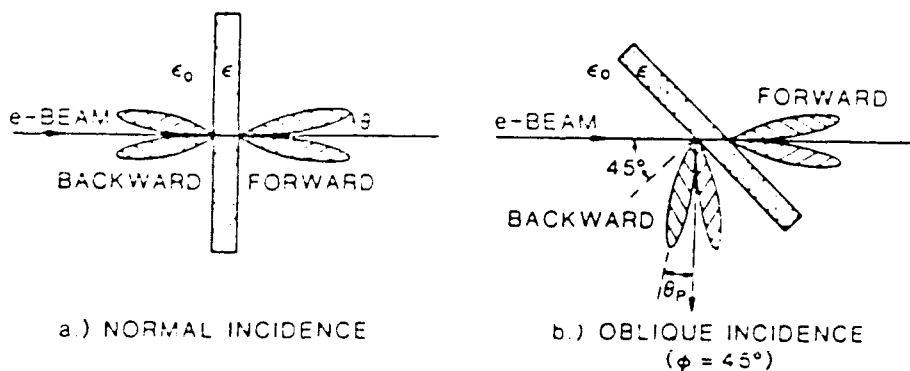


Figure 3: OTR patterns caused by an electron beam striking a target at both normal and oblique incidence. Figure (b) depicts the experimental approach used in this experiment.  $\phi$  is the angle of oblique incidence measured from the electron beam line to the foil. Note that the backward OTR is observed at the angle of specular reflection.

## B. PURPOSE FOR THE EXPERIMENTS

This thesis addresses two separate applications of transition radiation as a beam diagnostic at the Naval Postgraduate School (NPS) linear accelerator (linac) : measurement of the accelerator's beam emittance and the viability of a diffuse screen as a beam profile monitor. The application of transition radiation based techniques to determine beam emittance requires a detailed quantitative knowledge of the effect of beam divergence on the shape of the radiation patterns and on the polarization of the radiation; and whose calculations are beyond the scope of this paper [Ref. 3]. This paper presents the emittance measurement, procedure and lessons learned. LT Hellstern's future thesis will be to use the analytical expressions developed and tested using the Wartski interferometer method to determine the emittance of the NPS linac from the data measured in this work.

A novel OTR screen consisting of a surface purposely made diffuse was developed. The diffuse screen proved to be an excellent beam profile monitor. It accurately preserved the shape of the electron beam incident on the vacuum/metal interface to a viewing angle range of  $\pm 30$  degrees during the second of two experiments. The intensity of the transition radiation produced by electrons was also found to be a linear function of the current measured by a secondary emission monitor (SEM). The diffuse screen is an

inexpensive, easily constructed device which captures the actual beam profile and shape. For the purposes of this experiment, the diffuse screen was evaluated for angular and current dependence. It was compared to a front surface mirror producing convincing evidence of its efficacy as a profile monitor without the extreme viewing angle constraint of a mirror surface. The diffuse screen OTR response was also seen to be more linear with the current than with the use of a fluorescent screen.

## II. EMITTANCE MEASUREMENT

Until the relatively recent work done by Rule and Fiorito [Ref. 2], beam emittance measurements were time intensive, required heavy, non-portable equipment and cooling systems, and required beam transport models to accommodate measurements at multiple locations along the beam line. Using the properties of transition radiation, they developed a means of determining time-resolved beam emittance and energy measurements even for a single beam pulse. This chapter describes the application of transition radiation as a means of measuring the beam emittance of the NPS linac [Ref. 2].

Emittance measurements are made by focusing the electron beam to achieve a beam waist at the position of the scattering foils. When the beam waist is achieved, the root mean square (rms) local emittance is related to the rms beam divergence and the rms radius according to equation 3 [Ref. 4],

$$\epsilon = \theta_{rms} r_{rms} \quad (3)$$

Accordingly, this experiment consisted of establishing the data acquisition capability, optics alignment, and control of the electron beam to produce x and y waists at which to

measure the emittance. The beam divergence was measured by observing transition radiation and exploring its polarization properties.

The data acquisition devices used for the beam emittance measurement were the Hamamatsu Silicon Intensified Target Camera (SITCAM) and a Compaq Portable II MS DOS computer. The SITCAM consists of a highly light sensitive camera and a control unit with the capability to perform time integration and background subtraction of the signal. It also has the ability to make horizontal and vertical scans of the transition radiation interference pattern. A Cohu camera, model number 4815-5000, was used in the beam monitor experiment. The Cohu is a small, compact, solid state CCD camera sensitive to low intensity light. The interference pattern is created when the Wartski interferometer is used as the target. The interferometer consists of two parallel foils. In this experiment, Kapton was used as the first foil and produced forward transition radiation which coherently interfered with backward transition radiation produced by the second foil, a front surface mirror. The space between the foils was vacuum. The phase difference between the forward (produced by the first foil) and backward (from the second foil) transition radiation is given by the angle  $\phi$  which is equal to the separation of the foils along the electron path divided by the length of the radiation formation zone in vacuum (equation 4),

$$\lambda = \frac{2\pi L}{\beta\phi}(1 - \beta \cos \theta) \quad (4)$$

The width of the interferometer was chosen to correspond to the wavelength of the OTR selected for observation and the same order of magnitude as the length of the radiation formation zone in vacuum.  $L$ , the interferometer width, also determines the number of fringes in the interference pattern. As the width of the foil spacing approaches the length of the radiation formation zone, the interferometer produces more fringes and yields higher sensitivity to beam divergence [Ref. 5].

The optical alignment was performed by first determining the preferred path of the electron beam and causing the laser to follow the electron beam path. Convinced of their colinearity, the laser was used to align the optics. The Newport manufactured optical table in Figure 4 was designed to permit alignment of optical equipment in mounting holes. The cameras for both the emittance measurement and the diffuse screen experiment were mounted on the table. The Cohu camera was positioned to view images produced at the main scattering chamber from the diffuse screen experiment. The SITCAM captured the OTR images produced at the OTR chamber located downstream from the main chamber.

The alignment of the SITCAM was done using a 'focus-at-infinity' apparatus. The apparatus consisted of a



standard white light source projecting light through a neutral density filter assembly and aperture to a sector star target. The sector star target was a radial array of alternating opaque and transparent rays similar to a rising sun and is shown in Figure 5. The sector star image was focused through a two inch diameter lens and projected onto the face of the SITCAM lens. The focal plane was the plane at which the sector star was seen while the lens was focused at infinity permitting the viewing of the object as parallel light. The camera was then focused on the laser beam corresponding to the distance between the camera and the interferometer foil. This constituted a focus at the image plane as depicted in Figure 6. The SITCAM used a 135 mm lens and the Cohu camera used a 200 mm lens. Both lenses were chosen to capture the full OTR pattern within the selected bandwidth and to maximize the intensity.

Prior to performing the experiments, the different optical devices were calibrated. The SITCAM lens was calibrated with respect to the pixels on the computer screen. This was done by sweeping the left and right limits of the lens with a laser beam and measuring the relationship between the pixel position and the change in angle. This gave a horizontal angular calibration for the lens and was repeated along the vertical axis to give the vertical angular calibration. The camera was also calibrated to

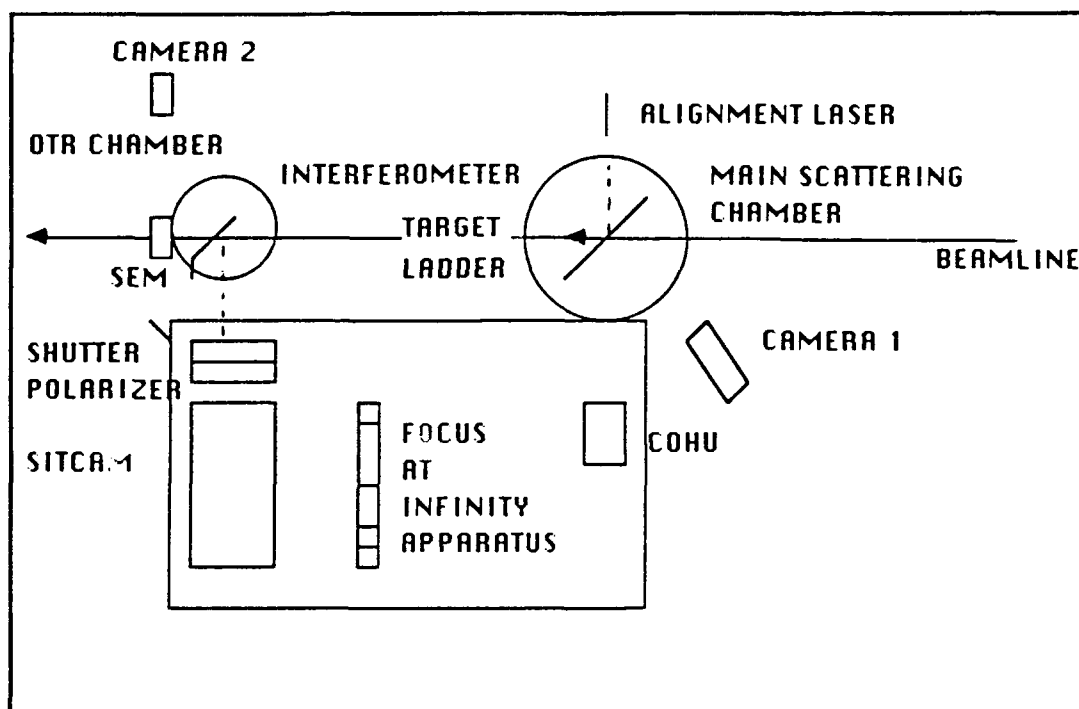


Figure 4: Equipment Setup. A Newport optical table is positioned parallel to the beamline. The SITCAM is positioned on the left side of the table to measure the emittance from the OTR chamber. The Cohu captures diffuse screen images from the main chamber on the right. Camera 1 was focused on the target ladder and camera 2 was focused on the SEM.

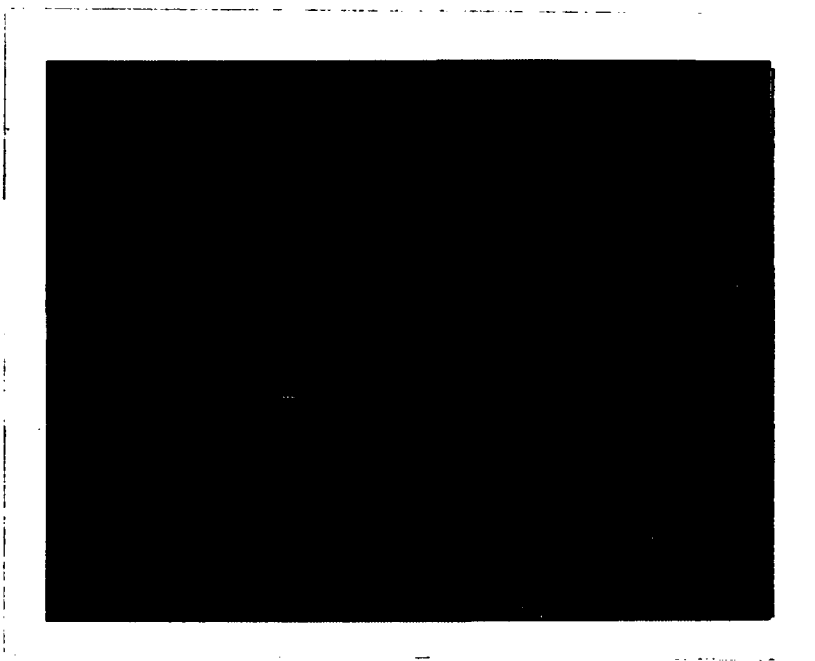


Figure 5: Sector Star Image. The image of the sector star as seen when captured by the SITCAM when the lens was focused to infinity. For a fuller description of its purpose and use, see Ref. 6.

## OPTICAL RAY DIAGRAM FOR OTR IMAGING

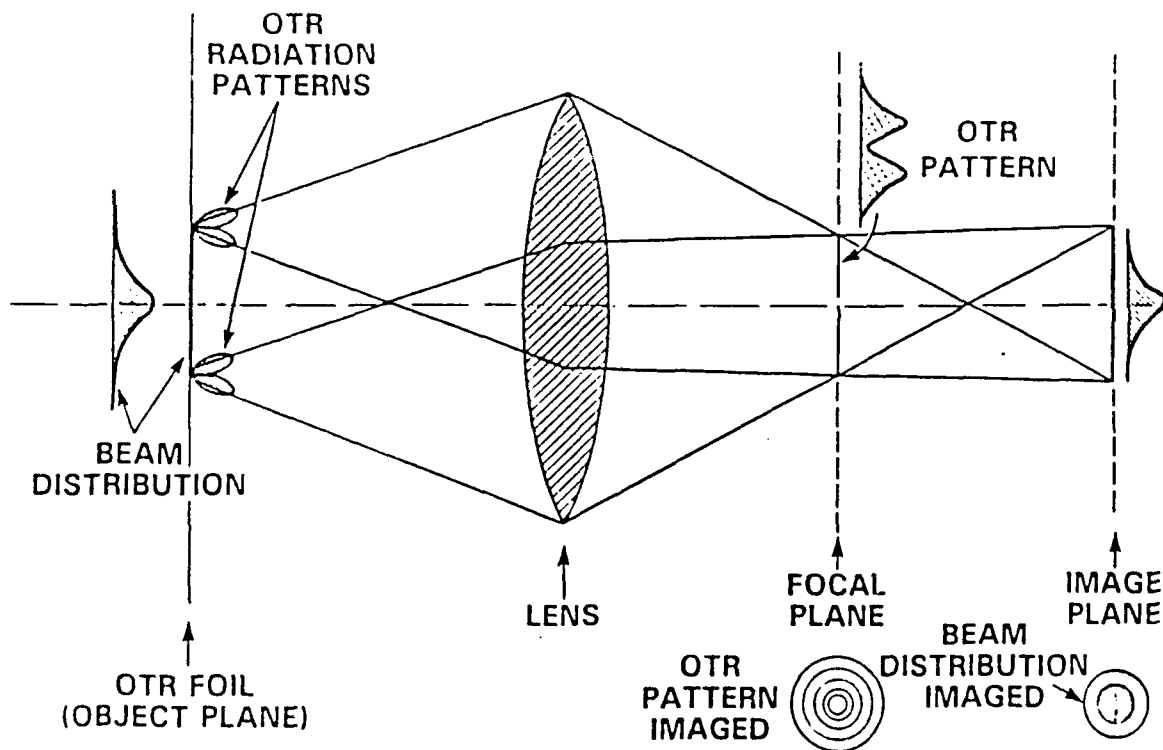


Figure 6: Optical Ray Diagram: The interference pattern is seen at the focal plane and the beam distribution is seen at the image plane.

relate the pixels in the x and y directions with real size of the captured images. This was done by observing a target grid of known dimension and measuring the picture image on the screen in terms of pixel location. The same procedure was followed for the Cohu camera using a marked fluorescent target in the ladder of the main scattering chamber.

Having established the data acquisition devices, aligning the optics and controlling the electron beam was done with the use of transition radiation. It was used to minimize fluctuations resulting in the most stable beam possible. The alignment was done by forcing the laser beam to follow the electron beam's path through a two point iterative procedure discussed in this chapter. The laser beam was then used to align the remainder of the optics. The accuracy with which they were aligned minimized asymmetries in the profile scans of the interference pattern captured by the camera. In the course of the experiment, the resolution of one problem revealed others until the linac provided a high quality beam. The key to solving these problems was the use of transition radiation as a real time monitor of the electron beam. The remainder of this chapter is a chronology of the experiment and the lessons learned.

#### **A. EXPERIMENTAL SET-UP**

The set-up for the emittance measurement experiment consisted of assembling the optical components on the

optical table, assembly of the optical transition radiation chamber and interferometer, and installation of data acquisition equipment within the control station. This section details the systematic procedure for acquiring data.

### **1. The Experimental Table**

The first step was to position the Newport optical table in order to support simultaneous observation of the main scattering chamber and the OTR chamber. The table was aligned parallel to the beam line in order to take advantage of the precision mounting holes in the table. Once in position, the OTR chamber was installed allowing positioning of the Hamamatsu SITCAM on the downstream side of the table. The Cohu camera was installed on the upstream side of the table permitting the capture of OTR images from the diffuse screen in the main scattering chamber (see Figure 4). The focus at infinity assembly was placed in the center of the table next to the angular calibration set-up. The focus-at-infinity device consists of a rail upon which an aperture, lens and sector star were assembled in front of a light source. Together, they projected light in the pattern of the sector star which would later be used to focus the camera at infinity (see Figure 6). The devices used to calibrate the lens consisted of a Newport laser positioned to the right of the light source, a mirror on a rotation station and a mirror in

front of the SITCAM at a 45 degree angle. These permitted the lens scan necessary to calibrate the 135 mm Vivitar lens being used on the SITCAM. The Vivitar lens was able to focus at both the focal and image planes. Just prior to the start of the experiment, shutters were positioned in front of each camera. Additionally, a polarizer was positioned in front of the SITCAM to be used to capture of horizontally and vertically polarized images.

## **2. The Optical Transition Radiation Chamber**

The Optical Transition Radiation (OTR) chamber was installed on a lab jack strong enough to support the weight of the chamber and along the beam line. A target grid the size of the mirror pellicle was constructed from graph paper, mounted on the mirror and used to assist in finding the location of the electron beam. This was done by first mounting a laser looking into the main scattering chamber opposite the optical table. Using a mirror in the main scattering chamber oriented at 45 degrees from the electron beam direction, the laser beam entering this chamber was reflected down to the OTR chamber. The lab jack was then adjusted for vertical position until the beam was in the center of the target grid (see Figure 4).

Once the camera was aligned with respect to the beam line, the Wartski interferometer was prepared for installation in the OTR chamber. The mirror and grid were removed from the chamber and graph paper discarded. The

interferometer was constructed of a thin Kapton film of thickness 0.003 inches and a silicon polished mirror finished pellicle. The thickness of the ring and Kapton together constituted the interferometer spacing which was .325 inches or 8.25 mm. Since the interferometer was oriented at a 45 degree angle for observation of backward OTR, the effective foil spacing was 11.6 mm. This spacing,  $L$ , is the distance along the beam path between the interferometer foils. The distance was chosen to be the same order of magnitude as the length of the radiation formation zone in vacuum. This distance is a function of the lorentz contraction causing the spacing to be given by equation 5 where  $L$  is the separation distance,  $L_v$  is the vacuum formation zone, and  $\gamma$  is the Lorentz factor,

$$L = L_v = \gamma^2 \lambda \quad (5)$$

The interferometer was then installed into the OTR chamber once the camera was aligned.

### 3. The Control Station

The data acquisition devices were all placed in the linac control station. These included the SITCAM computer, plotter and the Compaq computer used to store images and produce profile plots; the MacIntosh IIX computer using Image 1.29 and Pixelpipeline software; data recording polaroid cameras and video recorder; and monitors permitting



observation of the secondary emission monitor (SEM), main scattering chamber ladder, and the SITCAM. Oriel Encoder Mike controllers, model 18011, were also used to remotely control translation of the camera and the lens calibration rotation station. Another stepper controller was used to rotate the ladder within the main scattering chamber. A detailed discussion of the Image and Pixelpipeline software can be found in Chapter III in the discussion concerning the diffuse screen experiment.

#### **4. Aligning the Hamamatsu Camera**

The alignment of the SITCAM was a two man procedure begun after the initial set-up. The laser beam was confirmed to be going through the camera lens. This was an iterative procedure which determined the position of the camera and lens. Optical posts were temporarily positioned at the camera height to correspond to the locations of the front and rear of the Camera. The laser beam was then adjusted until the beam reflecting off the interferometer was seen touching the top center of each post. The camera was then installed at these post locations. Another target grid made of graph paper was placed inside a filter cap and placed on the camera lens. The lens and grid were adjusted by moving the camera until the laser was on the center of the lens target grid. This procedure established the location of the laser beam on the OTR mirror and the target grid on the lens filter of the SITCAM.

Next, the focal plane location was established. With all other lights turned off, a white light source was used to focus the camera lens at infinity (see Figure 7). Utilizing neutral density filters to assure that SITCAM would not be saturated, the position of the sector star was adjusted so that the star was focused. This was done by covering the bottom half of the star (exposing the top half only) and sliding the star forward and backward on a rail to locate the optimum focus position. Once found, the star was tightened in position. One mirror was placed in front of the infinity assembly at 45 degrees and another in front of the SITCAM to bring the star image into the camera lens. The lights were then turned off in the end station. The camera was turned on and adjustments made to the camera (moving the camera forward and backward on the rail) with the fine adjustment to bring the star into focus. This was done in the end station using a monitor while the camera operator observed the image from the control station using another monitor. Since both were observing the same picture on the monitor, the camera operator was able to confirm the observation within the end station. When both agreed that the sector star was at the position of maximum clarity and focus, the camera position was recorded as the focus at infinity position. The camera lens was then translated to the image plane. To establish the image plane focus, the

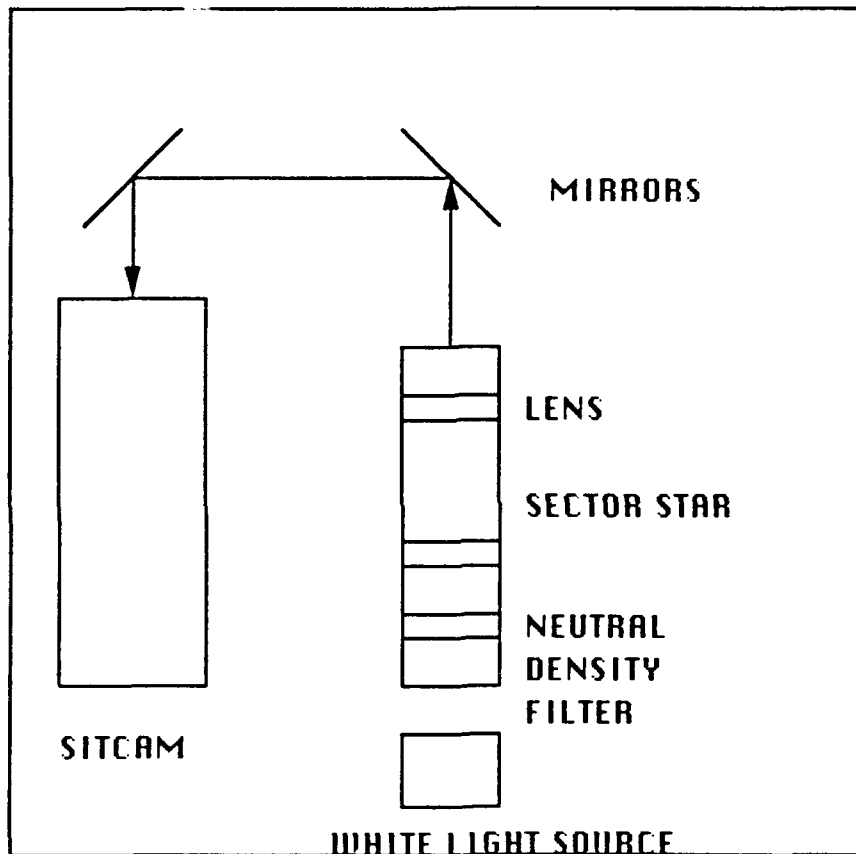


Figure 7: Focus-at-Infinity Assembly. This assembly was used to establish the focal plane location and focus. The white light projected the sector star image into the camera lens . The neutral density filters prevented camera saturation.

previously aligned laser beam was used. Once the laser beam spot was clearly focused, the camera lens position was recorded on the Oriel encorder. Together, these two procedures aligned the camera based on the assumption that the laser beam accurately followed the path of the electron beam.

#### **5. Angular and Distance Calibration**

The next step in the procedure was to calibrate the devices using the computer screen locations in pixels corresponding to angle and distance. These included the stepper calibrations for all translational controllers, the lens calibration and the target grid calibration. Whenever possible, the calibrations were made during set-up.

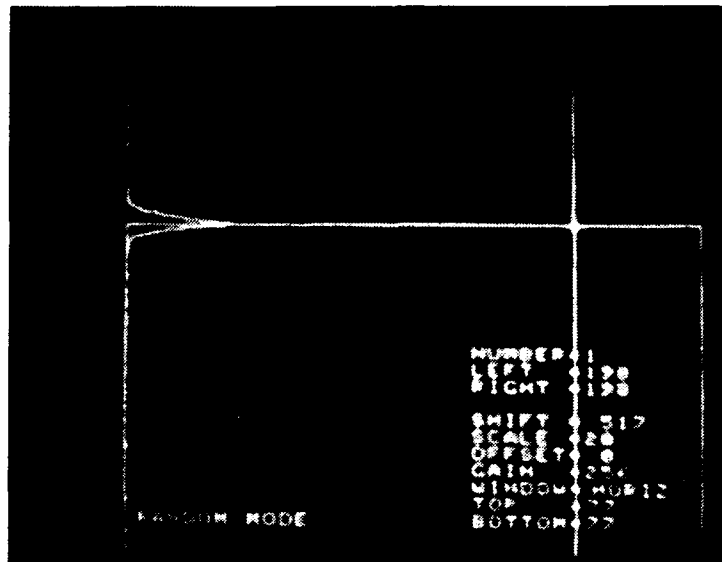
Calibrating the controllers was done by reading the outputs on the controller corresponding to the distance traveled on the associated vernier scales (measuring the true translated distance). For the lens calibration this meant initializing the controller at 0.0 and rotating the mirror so that the laser beam moved from one side of the lens to the next in intervals of 20 steps. The pixel position on the computer screen was recorded at each interval. The calibration lens scan was performed once in one direction and once in the reverse direction. Care was taken to provide for the effects of 'back lash' in the rotation station when the direction was reversed. Both lens scans were in excellent agreement. The results were then

plotted on graph paper. Fitting a straight curve gave a slope of 1.41 steps per pixel. This was converted to an angular relationship of 0.152 milliradians per pixel.

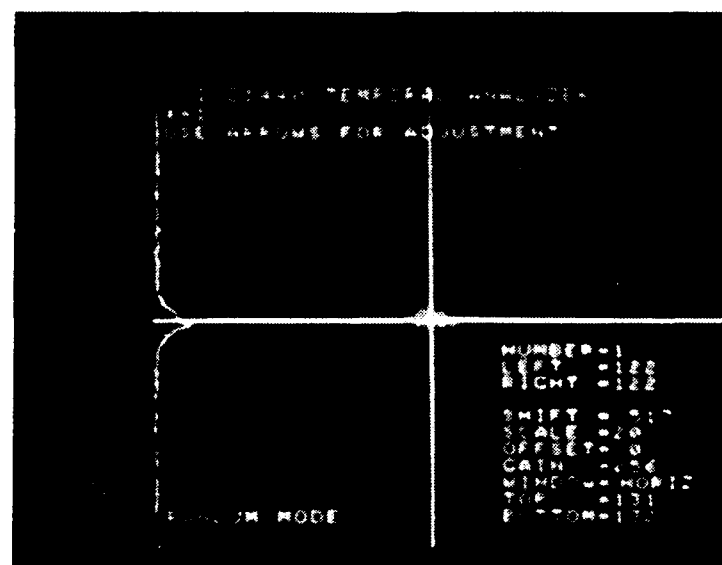
The vertical calibration procedure was a more involved process than the horizontal and produced slightly different results. The challenge in the setup was to limit the movement of the laser beam to a single plane. This was done by first positioning a laser perpendicular to the line formed by the camera and lens and parallel to the long side of the table. The laser was confirmed parallel by the same iterative procedure used to align the laser with the camera. A mirror was positioned to reflect the laser up and back toward the laser to the mirror on the rotation station. The rotating station was positioned between the laser and the first reflecting mirror at a distance equal to the distance of the camera lens to the center of the OTR chamber. The laser was used to verify that the rotation station was properly oriented by insuring that the laser was reflected onto the posts (previously used to make certain that the laser was parallel to the table). Satisfied of the proper orientation of the rotation station, the laser was reflected into the camera lens by another mirror. The retro-reflection off each mirror was a time-consuming, iterative procedure beginning with the laser onto the first reflecting mirror and finishing with the camera lens. The calibration was carried out in the same way as the

horizontal calibration. The lens was scanned from top to bottom using the laser beam. It was done twice producing consistent curves with a slope of 1.33 steps per pixel. This converted into an angular relationship of 0.144 milliradians per pixel. Comparing the horizontal to the vertical calibration gives a ratio of 1.06 : 1. Restated, the angular distance traveled along the horizontal axis (per pixel) was six percent greater than along the vertical axis.

The next calibration performed was comparing the number of pixels per millimeter in the horizontal and vertical directions. The image of the target grid made of graph paper was captured using the SITCAM. The width of each square on the paper was 12.7mm. The change in pixels corresponding to ten grid squares was recorded. The average horizontal calibration was 7.37 pixels per millimeter. The average vertical calibration was 10.2 pixels per millimeter. The magnification of the SITCAM as shown on the television monitor was accomplished by capturing the target made from graph paper with the SITCAM and photographing the image using the polaroid camera. The magnification of the polaroid image was calculated to be 1.92. The results of the horizontal and vertical angular and magnification calibration were an unexpected result. Initially, it was assumed that the camera response was identical in the horizontal and vertical directions.



(a)



(b)

Figure 8: Electron and Laser Beam Comparison. The top photograph (a) records the laser beam position used for aligning the optics as (198, 77) using the SITCAM crosshairs. The bottom (b) photograph shows the actual electron beam position of (122, 131).

## **B. THE EMITTANCE MEASUREMENT EXPERIMENT**

### **1. Beam Location Verification**

Verification of the laser beam focus position with the electron beam was the first step taken after completing the experimental setup (see Figure 8). This was done by turning the electron beam on and observing the OTR pattern at the image plane and subsequently at the focal plane. Looking at the image plane revealed that the electron beam was actually higher than the previously thought position as shown in the photograph contained in Figure 8b (which was the position previous work had indicated). End station steering was used to place the electron beam where the cross hairs corresponding to the laser beam had been established. When viewed at the focal plane, it was clear that the OTR radiation pattern was displaced. The conclusion was that the electron beam tended toward a different position than previously recorded and was unstable when an attempt was made to steer it to a position significantly different from that path. The following is the process followed to correct the problem. The first step taken to resolve the problem was to break the vacuum and determine the actual location of the electron beam from the burn spot on the Kapton interferometer. The burnspot was located at a position above and to the left of the center of the pellicle. This also suggested that the laser and electron beam were probably not parallel as had been assumed from previous



work. The interferometer was reinserted and the OTR chamber restored to high vacuum. Attempts to focus the electron beam did not help and the decision was made to determine where the beam tended to go and to cause the laser to follow this new beam path.

All steering was turned off and two points were defined as references to locate the beam. The first point was the fluorescent screen in the main scattering chamber. Only the vertical steering was used to move the electron beam to the center of the first point. The second point of reference was the center of the OTR foil (marked by the SITCAM cross hairs). Steering to the OTR foil took the beam slightly off the fluorescent screen and required steering back on the first point. Thus, after a few iterations, the beam was confirmed through the first point and a new location on the interferometer foil. This constituted a new beam path to be used for the experiment. The new electron beam location on the foil was to the left of the initial position at about the same height. Using the center of the foil as a reference, the new position was 12.48 mm to the right and 7.02 mm above.

The laser beam was then forced to follow this new path and subsequently used to realign the optics. The first step in adjusting the laser was to raise it to the height necessary to send the laser through the center of the fluorescent screen. Afterwards, the mirror was moved into

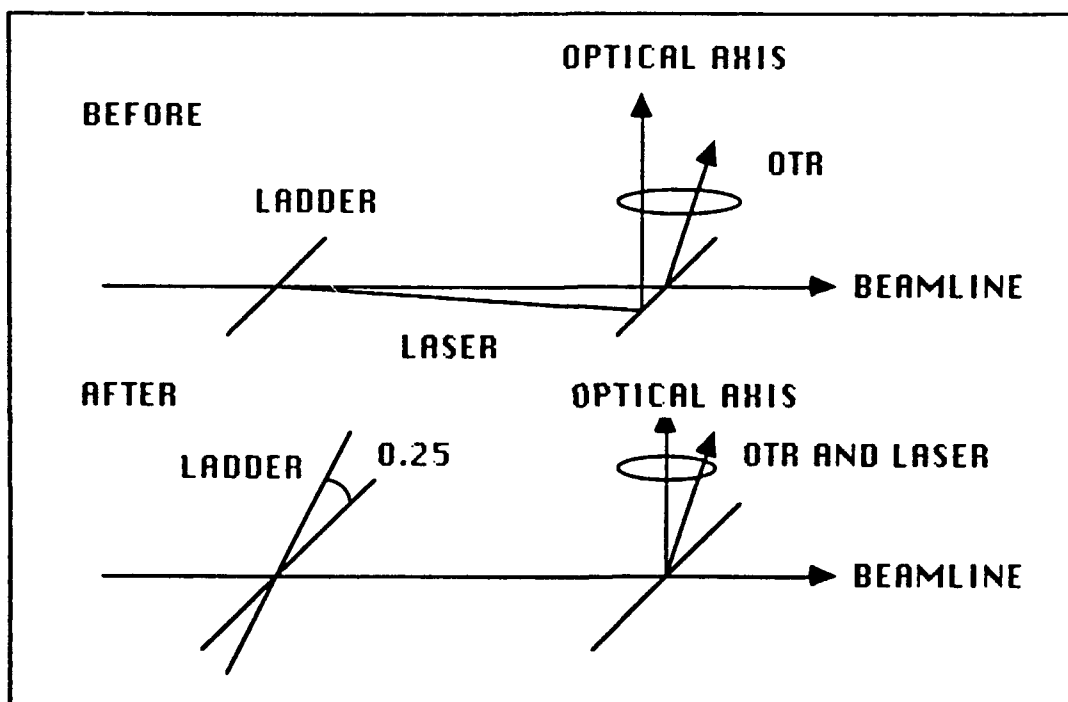


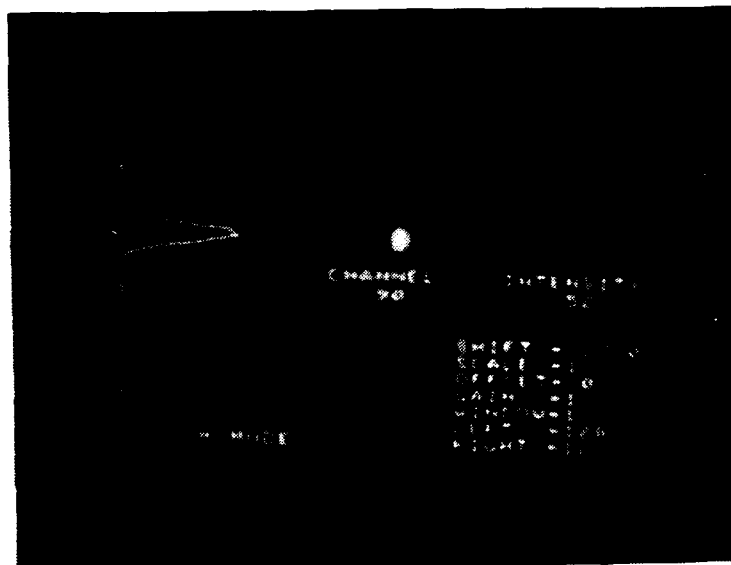
Figure 3: Colinear Adjustment of Laser. The laser was caused to follow the electron beam path and used to align the optics. After raising the laser height, the beam splitter positioned in the ladder was rotated 0.25 degrees to bring the laser on line with the electron beam.

position on the ladder and the laser was reflected downstream toward the OTR chamber. Having marked the pixel location for position of the electron beam using the SITCAM cross hairs, the ladder was rotated 54 steps resulting in a 0.25 degree rotation bringing the laser on line with the electron beam (see Figure 9). The colinearity of the electron beam and the laser was recorded using a polaroid photograph of a monitor. With the laser height readjusted, the remainder of the optics were realigned using the laser.

The procedure followed to locate the path of the electron beam and causing the laser to follow that path was clearly the best approach to take for establishing a reference with which to align the optics. On the following morning, the electron beam was found to be going through the first point on the fluorescent screen (pinhole). The beam was found to be going to nearly the same point on the OTR foil as the day before (marked by the SITCAM cross hairs). It was also clear that if the accelerator optics magnets were left on at the end of a run until the next use of the accelerator that the beam could be reproduced very well. (Overnight the beam deflection magnets were turned off.)

## **2. Data Acquisition**

After rechecking the alignment of the optics, the accelerator and camera were ready to begin capturing data to determine beam emittance. To begin, the camera was focused



(a)



(b)

Figure 10: Beam Distribution and Interference Pattern.  
 Figure (a) shows a fairly circular beam distribution.  
 Figure (b) shows the radiation pattern ( without the filter)  
 in was flat and wide. The energy slits were open to 0.25%.

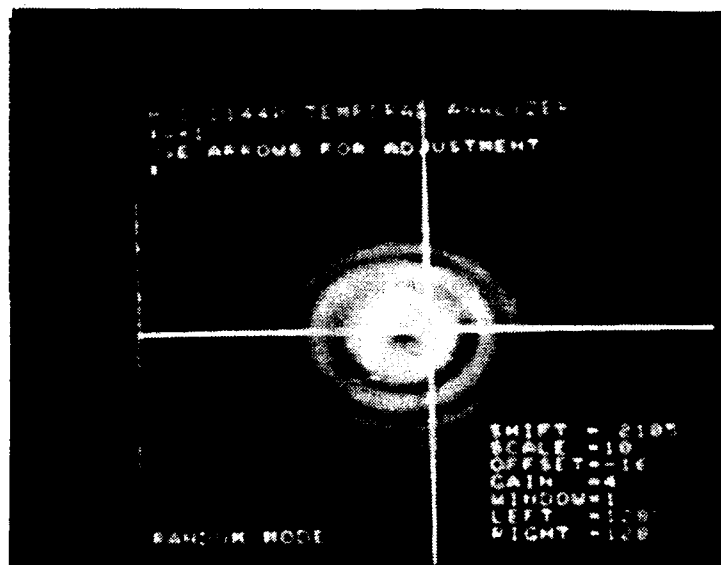
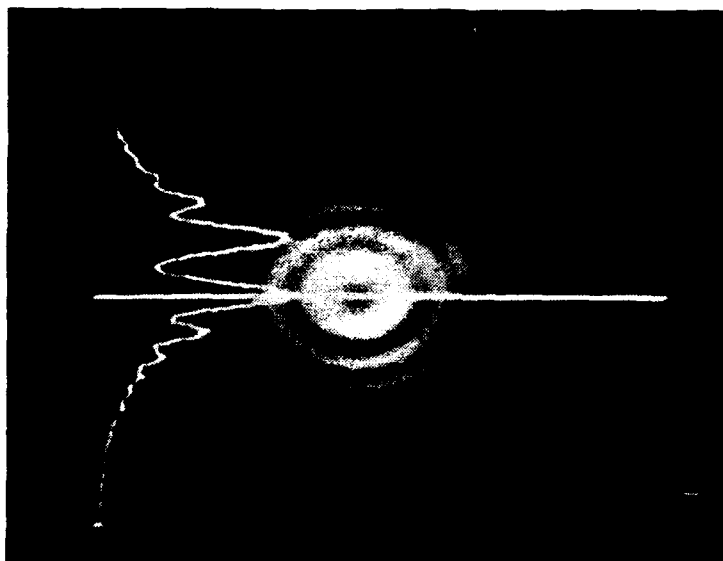


Figure 11: OTR Interference Pattern. The pattern is seen off center from where the crosshairs were recorded indicating the electron beam was coming in at an angle. The 50 nm bandpass filter was positioned between the camera and lens (quadrupoles were on).

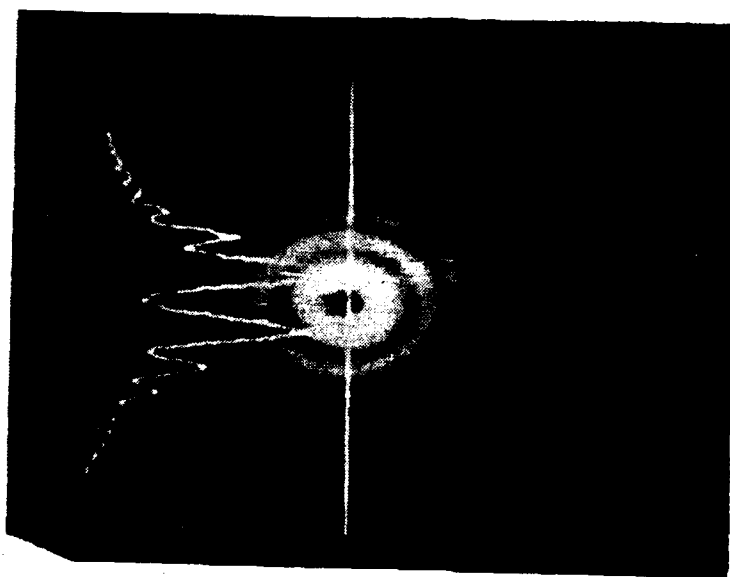
on the image plane to capture the OTR image. The image looked normal and was recorded (see Figure 10a). The camera was then focused at infinity to observe the bullseye without the presence of the bandpass filter (also referred to as an interference filter). The radiation pattern captured in Figure 10b was flat and wide due to electron beam energy spread. When the interference filter was placed between the camera and the lens, the interference pattern was seen clearly. The beam, however, was entering at an angle causing the interference pattern to be seen off center (see Figure 11). The beam focusing quadrupoles were then turned off. The next images captured were horizontal and vertical scans of the OTR interference pattern shown in Figure 12.

Studying the images captured to this point suggested that a problem existed with the optics or the electron beam. After considerable thought, it appeared that the effect of the interference filter had not been considered. The effective optical distance for the light given the presence of the interference filter was recalculated. This calculation led to adjustments in the position of the SITCAM lens for the focal and image planes. Confident of the correct position of the lens, the new positions on the Oriel encoder were recorded and the data collection resumed.

Measuring beam emittance must be done by capturing the OTR interference pattern caused by the electron beam incident on the interferometer at the x and y waists. The

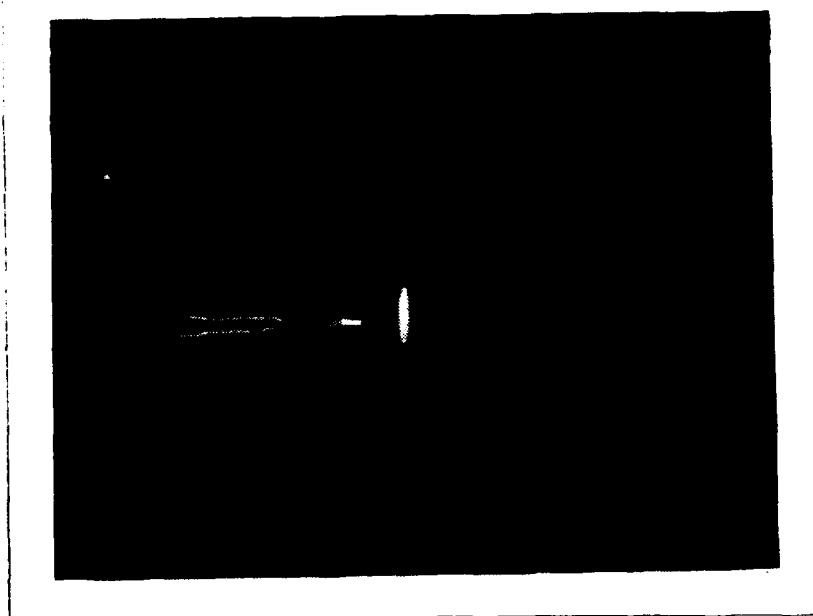


(a)

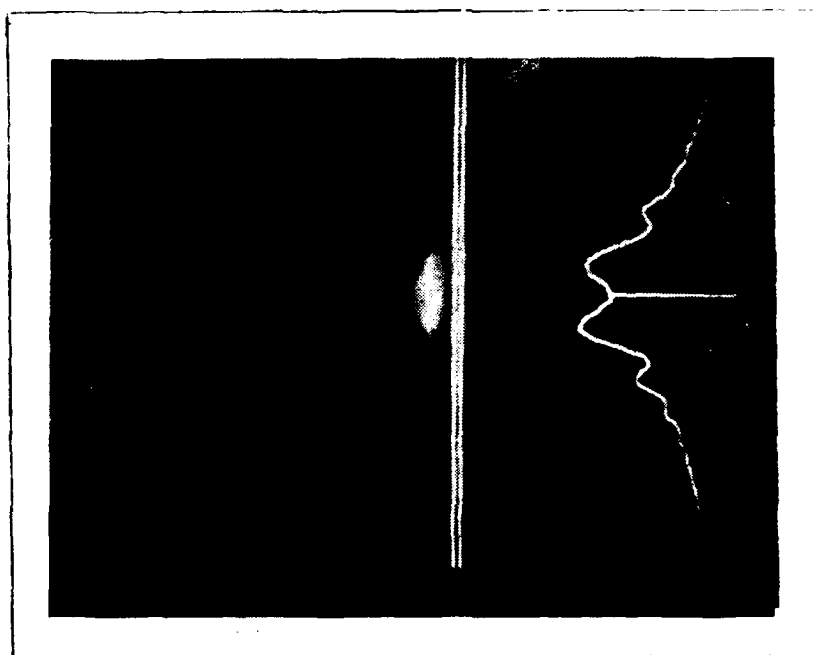


(b)

Figure 12: OTR Interference patterns. Figure (a) shows the horizontal scan of the interference pattern taken with the quadrupoles off. Figure (b) shows the vertical scan. The fringe patterns are numerous and vivid.



(a)



(b)

Figure 13: X Waist Images. Figure (a) shows the beam distribution for the x waist. Figure (b) shows the x waist interference pattern was displaced in the x direction and still seen flat and wide. The energy slits were still opened to 0.25%. A filter flare appeared for the first time.

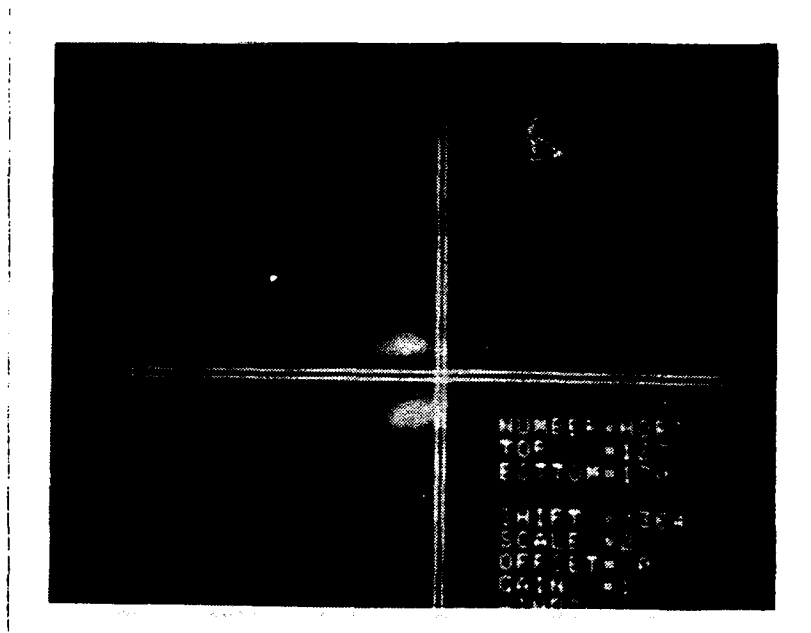


first images captured at the x waist are shown in Figure 13. Figure 13a captures at the OTR image while Figure 13b captures the radiation pattern at the focal plane with horizontal polarization. Two new problems appeared while focused at infinity. The image was displaced in the x direction suggesting an unstable beam and a flare appeared. Not certain as to the cause, the camera lens was returned to the image plane focus position where the image was clearly stable. The image, however, was in a different location. The computer cross hairs were used to mark the new location. The horizontal polarization was removed, beam focused and the image captured. The image appeared to be stable. This implied an optics problem. The first hypothesis assumed a reflection off the mirror or Kapton ring was going back upstream and reflected back again. This would suggest that the alignment of the beam with the optics was off by a few milliradians. The other hypothesis was that there was a trajectory problem. The beam might have been steering itself off the optical axis resulting in an angular displacement causing the interference pattern not to be in the center of the picture.

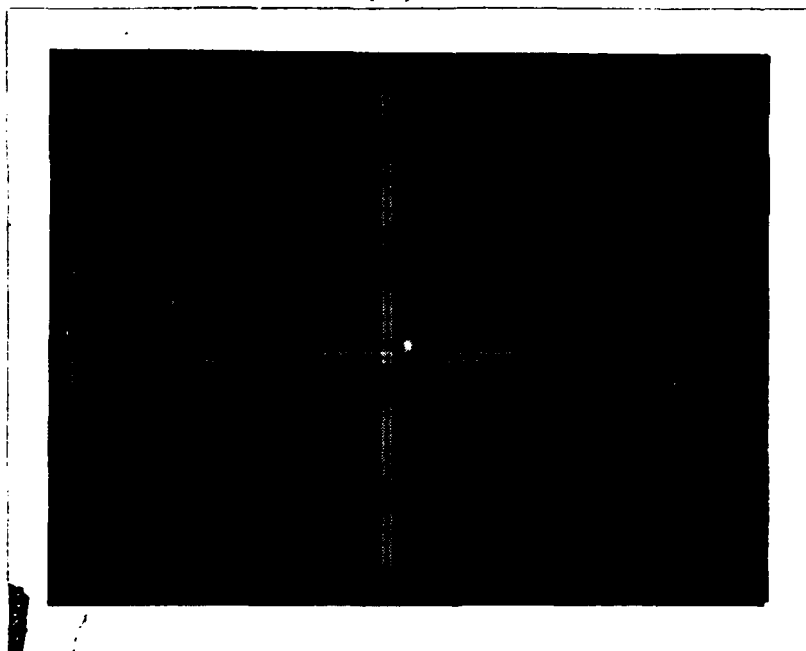
With those two hypotheses under consideration, another image was captured. Since the interference filter

was also suspect in the above mentioned difficulty, this image was taken without the filter. This new image seemed to supported the notion that the accelerator was producing a two component beam, each operating on its own unsynchronized pulse. The energy slits had been left open up to this point. The decision was made to minimize the effect by closing the slits down to an energy spread of 0.125% using the 1971 energy slit calibration performed on the linac [Ref. 7]. Reducing the energy slit width removed the flatness from the image as seen in Figure 15.

A comparison of images captured while focused at the image and focal planes was next made with respect to the cross hairs. The interference pattern visible when focused at infinity was to the left of the cross hair location (see Figure 14a). In contrast, the OTR image captured while focused at the image plane (Figure 14b) showed that the beam was to the right of the cross hairs at the image plane. The solution decided upon to correct the problem was to use the end station steering to return the beam spot to the cross hairs as seen at the image plane. Figure 15 captures the location of the electron beam after end station steering. The image focused at the image plane was brought on line with the cross hairs. The radiation pattern at infinity was still offset to the left (though less than before). The cause is uncertain. However, the combination of reducing

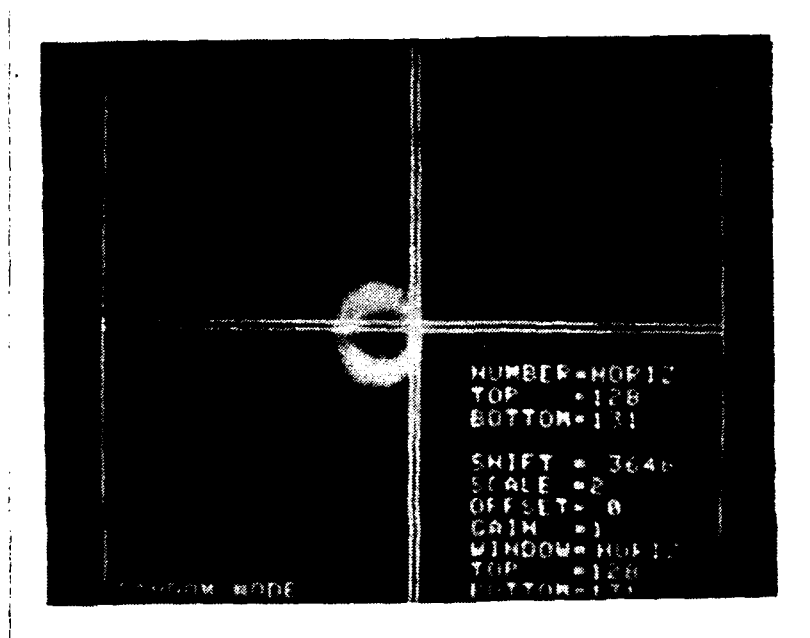


(a)

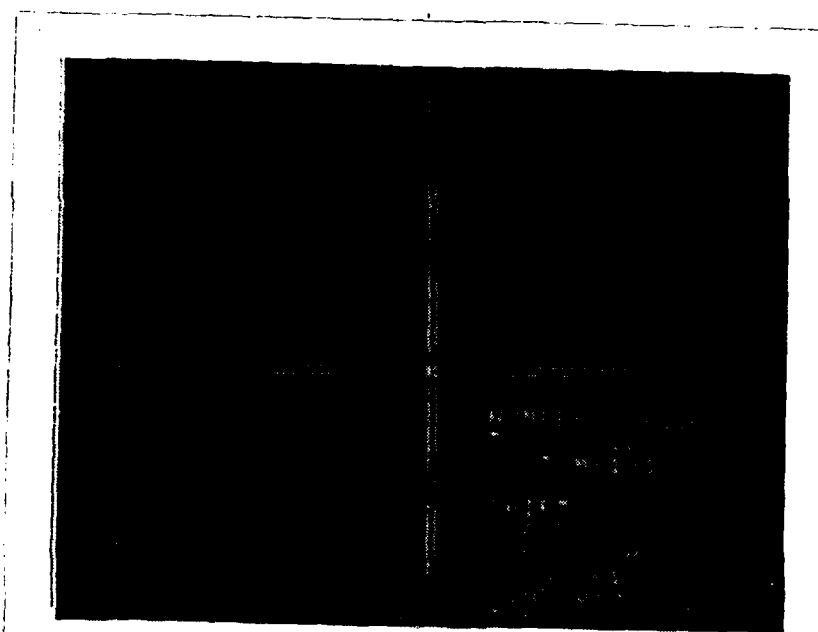


(b)

Figure 14: Effect of Closing Energy Slits. The energy slits were closed to 0.125% resulting in a focused, circular beam distribution and circular interference patterns. The interference filter was removed and the filter flare disappeared. Figure (a) shows the interference pattern to the left of center. Figure (b) shows the beam distribution to the right of center.

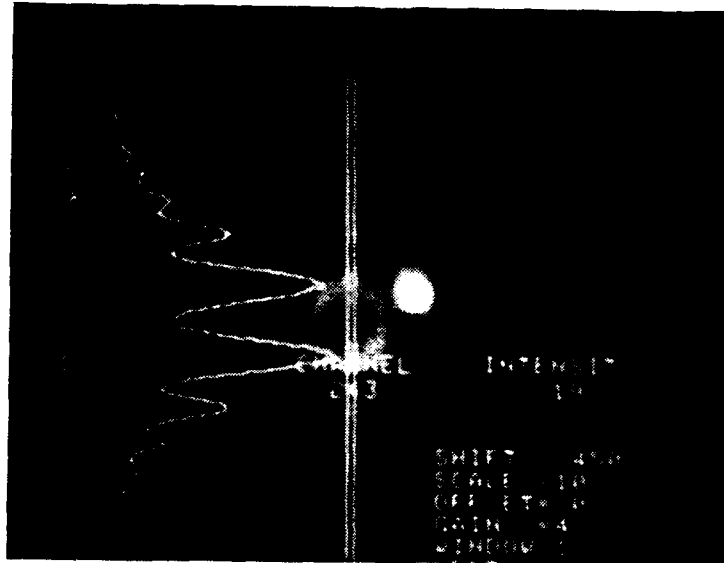


(a)

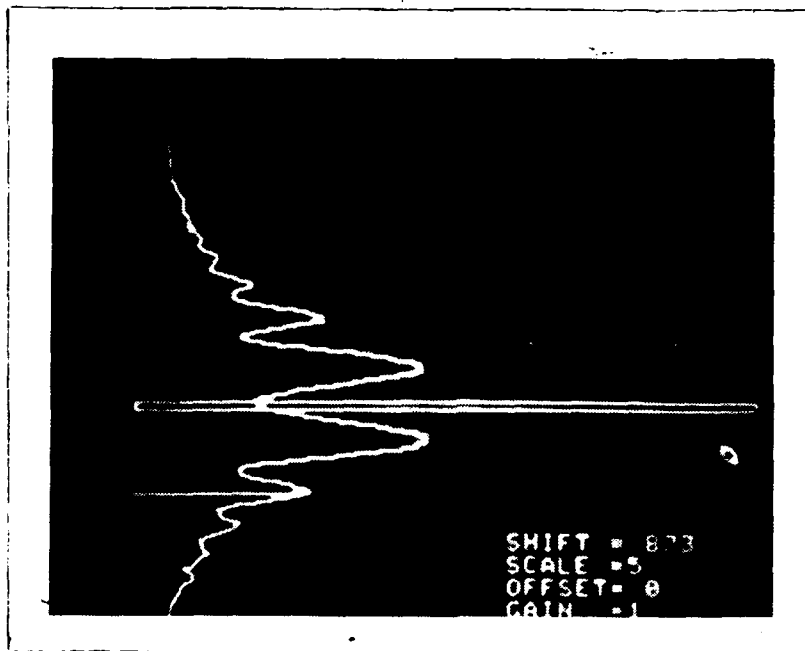


(b)

Figure 15: Effect of end station Steering. The end station steering was used to bring the beam distribution back to the cross hairs. Figure (a) shows that steering did not affect the interference pattern. Figure (b) shows that the beam distribution was centered.



(a)



(b)

Figure 16: Filter Flare Movement. The slight displacement of the interference filter dramatically changed the location and shape of the filter flare. The position of the filter permitted light to be reflected upstream and refocused into the lens. Figure (a) shows the flare before displacement. Figure (b) shows the flare after displacement.

the slit width and end station steering removed the effects of the unstable electron beam in the x direction.

Having returned the electron beam to its original position using end station steering, the interference filter was replaced between the camera and the lens. The interference filter was a 5950-6050 Angstrom bandpass filter. The image in Figure 16a revealed yet another problem with the re-introduction of the filter. A filter flare was clearly visible to the right of the image. It was initially thought to be stray light. Measures were taken to cover potential sources of stray light in the end station which did not alleviate the problem. Another image was captured and found to be markedly inhomogeneous. Again the hypotheses of an unstable, two component beam and reflected upstream light were evaluated. But the cause proved to be the interference filter. This was done by positioning the filter at a slight angle on the camera face. When the next image was captured, the filter flare had moved. A number of explanations were studied. The most plausible seemed to be that the location of the filter between the camera face and the lens permitted a reflection of stray light off the filter back to the interferometer and back into the lens focused at the image plane resulting in a clearly focused and well defined flare on the screen. Thus, as the filter was displaced, so was the flare resulting from the reflected light. The solution was to position the filter in front of

the camera lens eliminating the filter flare. Figure 16b shows the image captured after repositioning the interference filter.

As had been the case above, resolving one problem exposed others. In this instance, the addition of the polarizer caused difficulties. The polarizer severely reduced the amount of light which actually made it to the lens and made it difficult to produce a good, clear image. The 50 nm bandpass filter did not pass photons with long enough wavelengths to produce the light intensity necessary for clear, vivid images. A 6328 Angstrom filter was substituted but was also found to be insufficient. The solution was found by observing short wavelength light with a Corning 428 nm blue green 100 nm bandwidth filter.

Transition radiation also served to help maximize the quality of the linac's electron beam. The OTR foil was used as a beam monitor to help diagnose problems and find solutions, when possible. An example was the shape of the electron beam at higher currents. The OTR image produced at a y-waist was captured while focused at the image plane. The Figure 17 shows that the electron beam has tails which become increasingly visible as currents are raised. In order to measure the y-emittance, the electron beam was focused in the y direction at the camera object point on the OTR foils. The x direction beam would ideally be unfocused. However, this had an effect on the y spread of the beam.

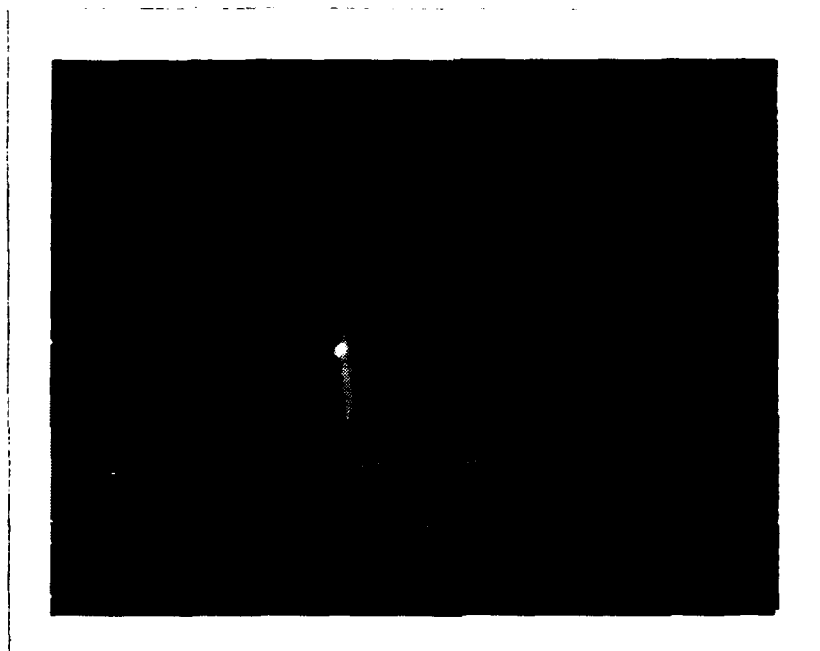
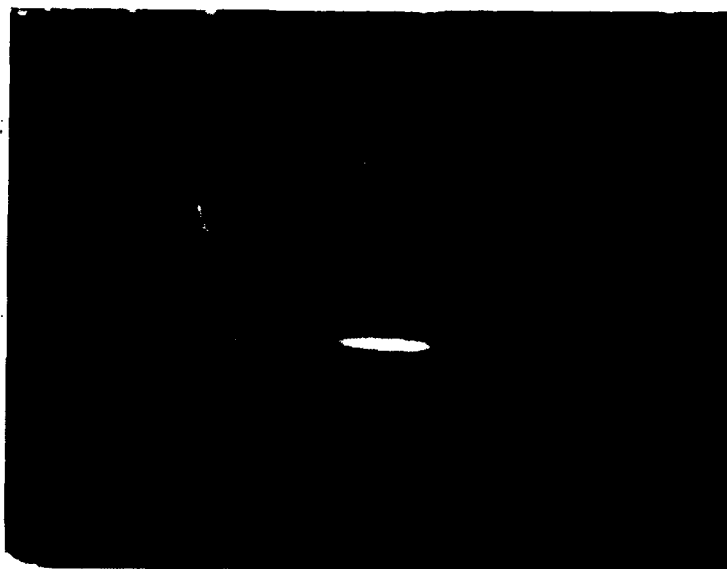
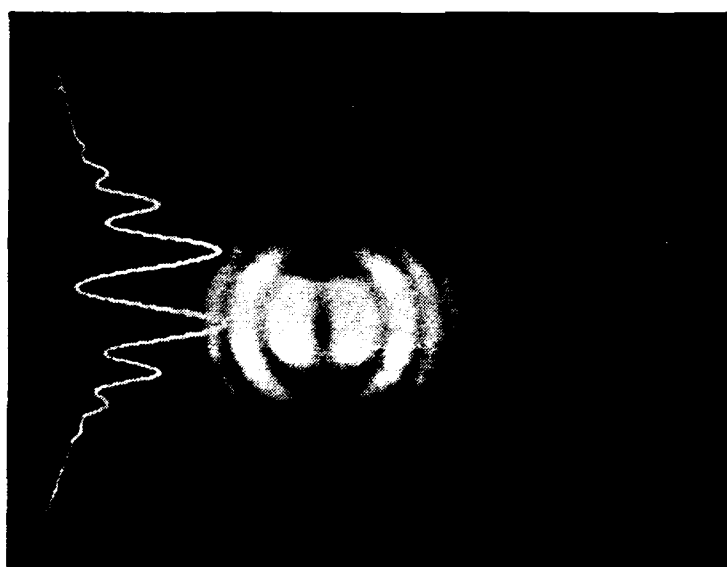


Figure 17: Beam Distribution using Corning 428 Filter. The use of the Corning 428 nm filter permitted the passage of enough light to make the tails of the electron beam visible at higher currents.





(a)

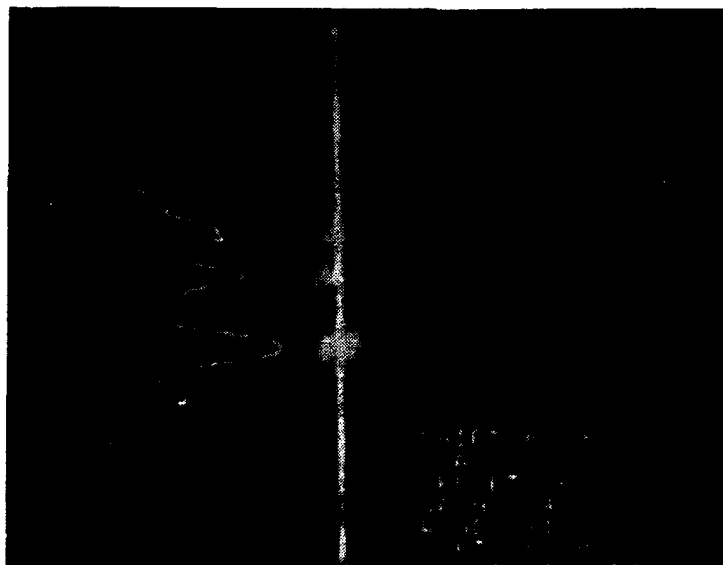


(b)

Figure 18: Y Waist Images. Figure (a) shows the y waist at the image plane. Figure (b) shows the presence of the filter caused some polarization in the interference pattern seen at the focal plane.



(a)



(b)

Figure 19: Polarization of the Y Waist. The photographs show vertical scans of the horizontal polarization in Figure (a) and vertical polarization in Figure (b).

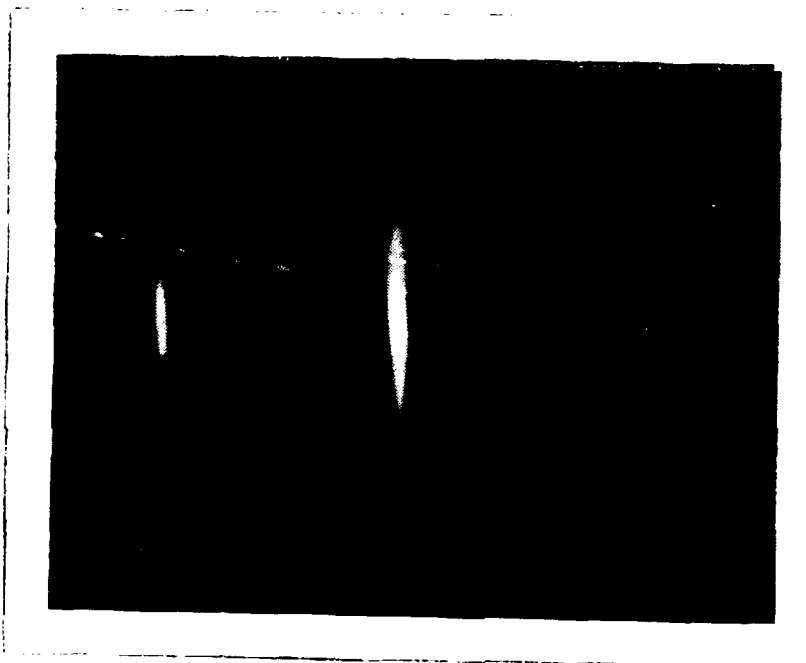
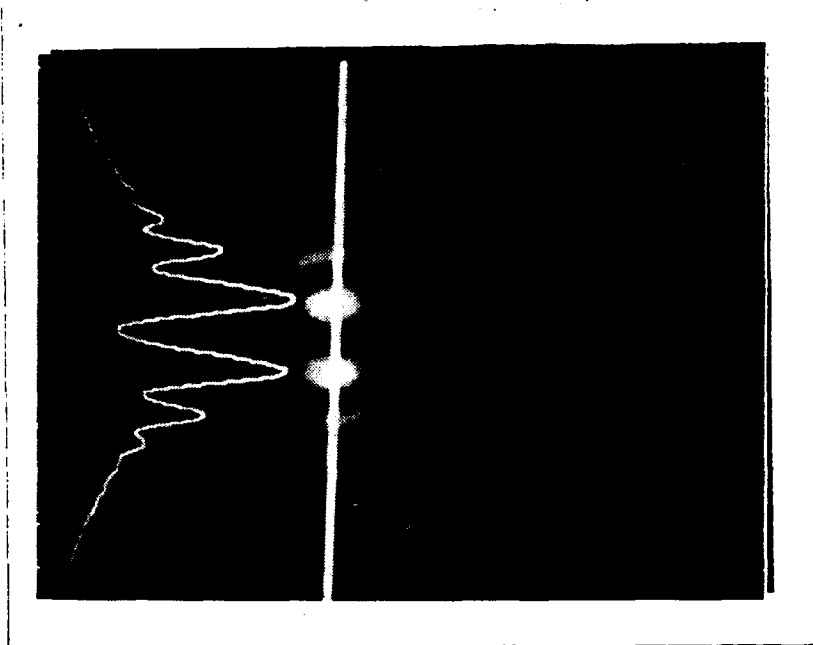


Figure 20: Satellite Images: Multiple 'satellite' images were visible when observing the x waist resulting from reflections off the OTR window and the OTR mirror of the interferometer. The outer images were blocked using black construction paper.

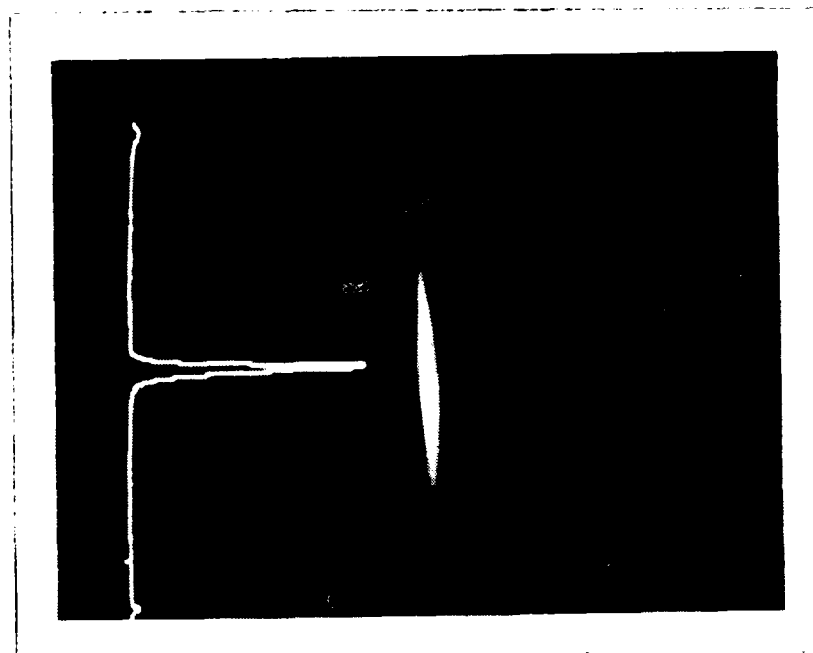
The narrowest y extent was obtained by slightly under-focusing the x quadrupoles. The y-waist was captured while focused at the image plane and is shown in Figure 18. Figure 19 contains vertical scans of the horizontal and vertical polarized OTR interference patterns of the y-waist.

When an attempt was made to obtain the x waist image, multiple images of the beam spot were the result of reflections from the chamber windows and the OTR mirror target. These are flares due to the experimental arrangement of various reflecting surfaces (see Figure 20). To eliminate these flares, pieces of black construction paper were positioned on the window to block the left and right images leaving the primary image in the center. An accelerator frequency dependent vertical displacement appeared at this point in the experiment. Study of the beam and the construction of the accelerator sections suggests that the misalignment of the three linac sections resulted in vertical movement in the beam which was accelerator frequency dependent. Attempts were made to minimize the effects of this problem with limited success.

Figure 21 shows the image and focal plane OTR images for the vertically polarized x-waist. The fringe patterns are also shown for the vertical scans of both images.



(a)



(b)

Figure 21: X Waist OTR Patterns. Figure (a) shows the beam distribution. Figure (b) shows the interference pattern. Both are shown with vertical polarization.

Figures 22 and 23 show the horizontally polarized x-waist photographs and their horizontal and vertical scans. The data taken as Figures 18, 19, 21, 22 and 23 will be analyzed in a subsequent student thesis to determine the emittance of the NPS linac.

The procedure and chronology contained in this chapter give more evidence of the utility of transition radiation as a beam diagnostic and monitor. OTR was used to verify correct optical alignment, identify erratic beam behavior, and optimize the beam to make excellent emittance measurements. The photographs contained in this chapter demonstrate the clarity with which OTR can be seen and measured by following the setup procedure contained within.

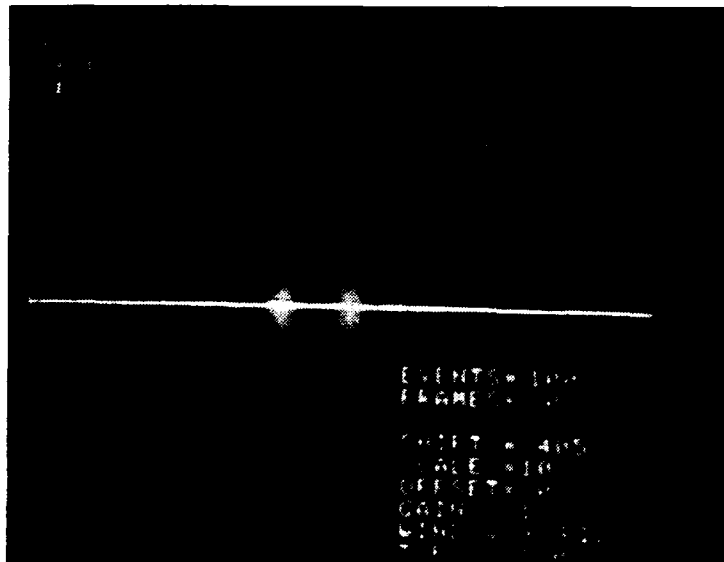
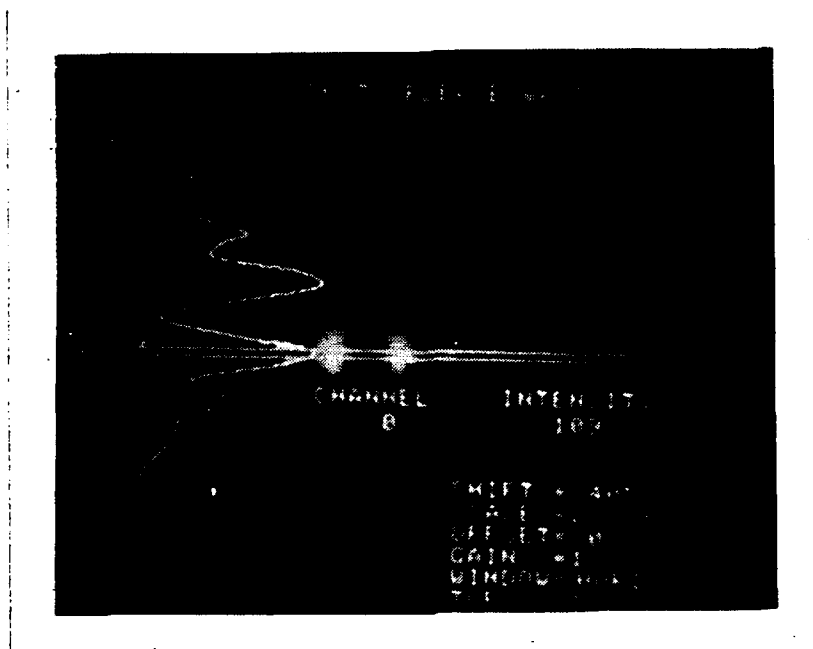
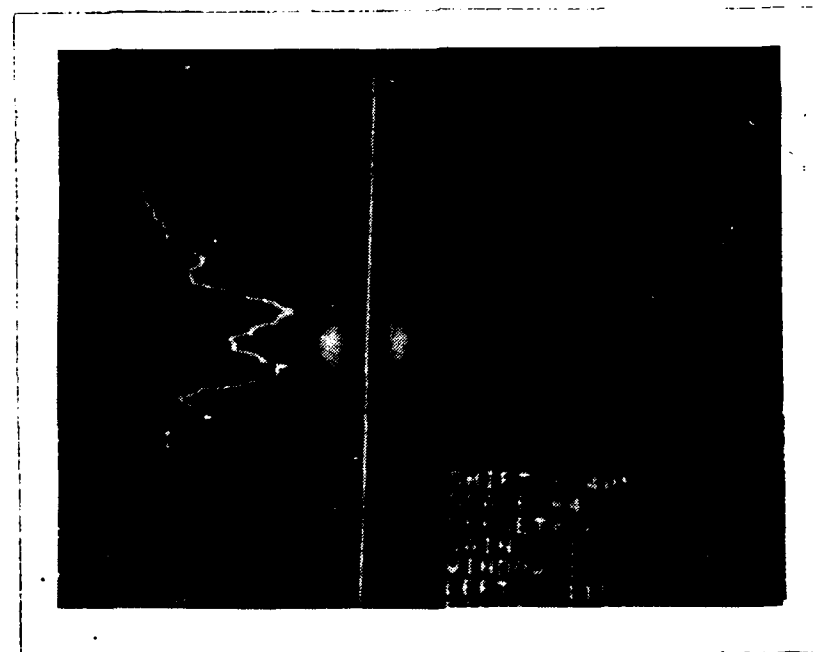


Figure 22: X Waist OTR Pattern. The interference pattern is shown experiencing horizontal polarization.



(a)



(b)

Figure 23: X Waist OTR Patterns. Figure (a) shows the fringe pattern and horizontal scan of the horizontally polarized image. Figure (b) shows the fringe pattern and vertical scan of the same image.

### III. THE PROFILE MONITOR EXPERIMENT

The need to profile the electron beam of an accelerator is critical in many experiments. The purpose of this chapter is to present the experimental method followed in two experiments in which the beam profile was measured as a function of the angle of orientation of a diffuse screen with respect to the electron beam. The diffuse screen is a foil of aluminum which was sandblasted to cause an uneven surface. Because there are many angles of specular reflection for this screen, OTR can be observed over a wider range of screen orientations than would be possible with a mirror surface screen. The diffuse screen was compared to a front surface mirror and fluorescent screen for angle and current dependence. Analysis of the data acquired during the experiments suggests that the diffuse screen is an excellent beam profile monitor capitalizing on the nature of optical transition radiation. The principle feature is its relative constancy in maintaining the beam shape over an observation range of at least  $\pm 30.0$  degrees (see Figure 32). The actual limits of the angular rotation could not be tested during these experiments due to the geometric limitations of the diffuse screen in the ladder. Based on the excellent intensity and profile shape of the image at the  $30.0$  degree rotation, there is every reason to believe that the actual



limits may be extended to around  $\pm 40$  degrees. The diffuse screen was also shown to increase the range over which the intensity of the OTR pattern is visible when maintaining a constant current dependence. The diffuse screen was also less sensitive to electron beam fluctuations when studying both angle and current. Because the OTR from a mirror is concentrated at a particular angle, it is easy to saturate the OTR image from a mirror. With a diffuse screen, the intensity is considerably less. When the angles were increased, the current had to be increased to capture images. The diffuse screen also is easily and inexpensively constructed and employed. Lastly, the diffuse screen does not produce secondary electron effects from the incident electron beam causing the OTR pattern to give a false representation of the electron beam profile (as in the case of the fluorescent screen).

The following sections of this chapter discuss the experimental procedure and lessons learned about the data acquisition equipment and software. The first section describes the experimental setup of the Cohu, a small, compact, solid state, monochrome CCD camera sensitive to low intensity light [Ref. 8]. The alignment and calibration of the camera was done using the target ladder housed in the main scattering chamber. The ladder contained the beam splitter to split the laser beam for alignment, a fluorescent screen with bullseye for calibration and

measurements, and a front surface mirror and diffuse screen made of aluminum. The computer software section follows the setup. This section discusses the two principal programs used to capture and analyze data: Pixelpipeline and Image 1.29, respectively. Pixelpipeline is a commercially marketed frame grabber board and software designed to work with the National Institute of Health (NIH) distributed software, Image 1.29. For the purposes of this experiment, the 'integrate' option of Pixelpipeline was used to enhance the OTR images. The background noise was subtracted using the background subtract option of Image 1.29. The final section discusses the actual experiment and procedure.

#### **A. THE DIFFUSE SCREEN EXPERIMENTAL SETUP**

The set-up of the Cohu camera was much less complex than for Hamamatsu SITCAM. The camera was leveled and positioned 11.25 inches from the lens cap to the metal rim of the chamber window (see Figure 24). The Canon 200 mm lens was focused at the image plane during the set-up and included a spacer between the lens and the camera. The lens focus was 5.5 on the meter scale. A beam splitter (on the target ladder) was positioned allowing the laser located on the opposite side of the scattering chamber to pass through. The laser beam was used to align the Cohu camera. The laser was retro-reflected off a mirror attached to a microscope

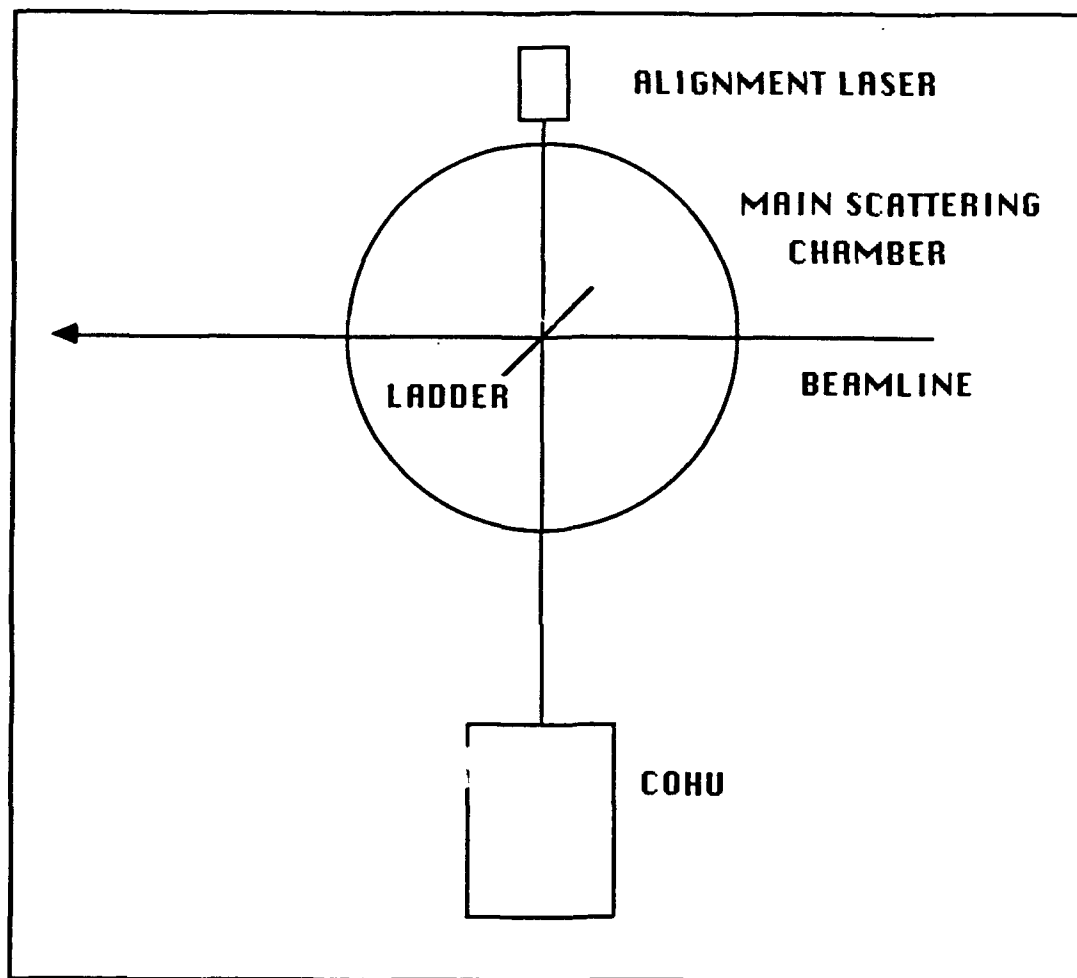


Figure 24: Cohu Camera Position. The Cohu camera was aligned using the alignment laser to observe OTR from the diffuse screen, mirror and fluorescent targets in the main scattering chamber.

slide on the front of the Cohu lens. That completed the alignment of the Cohu. The diffuse screen was inserted into the target ladder insuring that the diffuse surface would face the electron beam when the ladder was oriented at 45 degrees to the beam. Care was also taken to insure the diffuse surface was in the center of rotation of the target ladder. The camera and shutter were controlled remotely from the control station. The computer used to rotate the ladder was calibrated at 213.475 steps per degree. The Pixelpipeline computer card was installed into the Macintosh IIX computer and tested. The camera was calibrated by capturing the image of the fluorescent screen with the Cohu and measuring the pixel positions on the computer screen. These were compared to the actual distances on the screen and gave the following results: the horizontal and vertical calibration were 15.69 and 21.77 pixels per millimeter, respectively. From these calibrations, in principle, 100 micron resolution is readily obtainable with this system.

## **B. COMPUTER SOFTWARE**

The analysis of the data collected during the diffuse screen experiment was done using the most recent version of the NIH distributed Image software entitled Image 1.29. The data analysis should have been simplified by the use of the recently acquired Pixelpipeline software from the Pixeltools family of applications. Pixelpipeline provides several new options for collecting data in real time. The options of

interest to this experiment were 'integrate' and 'background subtract'. Integration takes what otherwise might be an unimpressive image and produces a clear, distinct pattern distinguishing the signal from its surroundings. For the purposes of observing OTR, this means the accumulation of light intensity over time. The background subtract option provides for the subtraction of the background while capturing an image. This is done by capturing an image of the background during 'live video' and placing it in the secondary buffer. Once placed in the secondary buffer, it is automatically subtracted from future incoming images when the background subtract option is selected. The reason these capabilities were not used was due to the way in which the software was written. The software does not permit the combining of any two options simultaneously. This can be corrected by purchasing another applications package from the manufacturer that provides the user the capability to alter the software to perform both operations simultaneously. Consequently, the decision was made to use the integrate option to capture OTR images using Pixelpipeline and use the background subtract feature of the Image 1.29 software. The background subtract feature is not specifically referred to as such in the Image software instructions. The procedure is found under 'Show Paste Control' of the Image software instructions [Ref. 8]. The paste control window is presented on the screen when

selected from the Options menu. It is there that subtraction of the background image from the image containing the signal is performed. Due the Pixelpipeline software limitations, images had to be integrated using one package and the background subtract was done using another.

After determining the above limitations of Pixelpipeline, subsequent conversations with the software designer revealed what was suspected but not confirmed. The Pixelpipeline software was specifically designed to work with the Image Software. Consequently, no analysis capabilities were written into the program. The analysis of images using Image 1.29, however, is dependant largely on how the captured images are saved. The Pixelpipeline manual provides several options under which to save images ranging from the standard TIFF header to the PICT header. But it does not specify the ramifications of saving under one format or another. Telephone conversations again clarified that the integrated option creates a 16 bit image while ordinary live video options create eight bit images. When saved, however, the image is only stored as an eight bit image. To specify the eight usable bits, integrated images must be saved under the TIFF, Simple format.

### Image 1.29

Image 1.29 provides for both qualitative and quantitative analysis of digitized products. The qualitative options used in this experiment included the three dimensional plot and the line profile. These gave information on the shape of the OTR pattern produced by the electron beam on the mirror, and diffuse and fluorescent screens. The quantitative tools of Image 1.29 used in this experiment included Integrated Density, Mean Density and Column Average Plot. These options did not all produce useful information. The only quantitative tool to measure OTR image intensity that proved to be consistent was Mean Density. The following section addresses those findings.

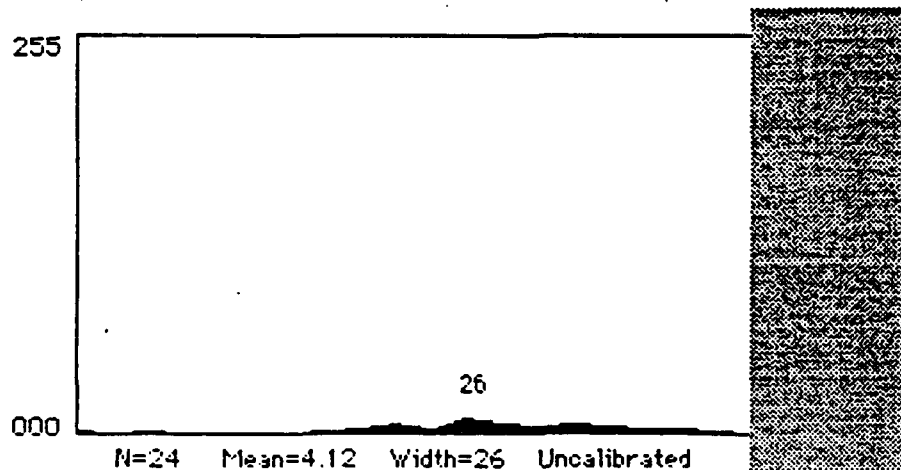
Part of the analysis of the data acquired during the diffuse screen experiment required knowing the intensity of the OTR signal created by the electron beam on the various surfaces. The first option tried was the Column Plot Average. When the rectangle tool is used and an area is selected for analysis, the Column Plot Average function causes all pixel values for intensity within a column to be averaged producing a profile plot. The curve produced can be compared with other images qualitatively for shape assuming that the areas of interest (rectangles) were fixed and covered the same pixel locations. Quantitative comparisons are also possible. This is done by measuring the area under the curve. The procedure for measuring the

area was found in the software instructions under Analyzing Electrophoric Gels [Ref. 8]. The procedure was clear but produced highly inconsistent results. There were two principal problems that fall under the category of inconsistency. The first was that the area was calculated with two different equations. One calculated areas on the order of ten, twenty or fifty. The other calculated numbers on the order of thousands. These calculations failed to follow any perceivable set of operator actions. The second problem was that the numbers did not seem to correspond to the relative sizes of areas represented under the curves. Figure 25 shows two examples of area under the curve demonstrating this inconsistency. At unpredictable instances, an area of lesser dimensions sometimes was assigned a larger value than areas of much larger dimensions. After a series of measurements, the problem was found to lie in the code that calculates the area and not that which calculates the curve. The curve dimensions seemed to correspond closely with the easily discernible image intensities on the computer screen. But the calculated areas did not. Consequently, the Column Plot Average was useful only in comparing the relative shapes and sizes of the curves representing pixel intensities when averaged within a column.

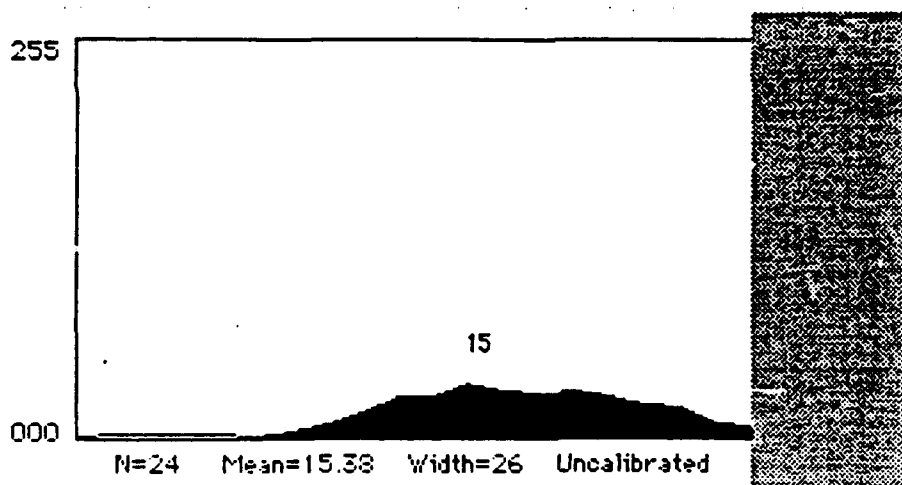


The next option available was the Integrated Density function described on page 24 of the software instructions. Specifying Measure under the Analyze menu causes items specified in the Options box to be measured. This was immeasurably more simple and faster than the Column Plot Average approach to measuring the area under the curve. However, this also produced unacceptable inconsistencies. Data analyzed using this function produced results that deviated too far from what was expected indicating a discrepancy in the computer code used to calculate the integrated density. Several attempts were made to vary the size of the area of interest. But that did not solve the problem. Previous work included the subtraction of equivalent sized areas of interest as background from the signal which reduced the scatter somewhat to around 10%. The problem with that method seems to be the wide variance of background noise from one part of the screen to another. Thus, the likelihood of subtracting the actual background noise from the image is fairly remote. The next step taken to address this problem was to take the equation discussed in the manual and compute the integrated density manually. The results are shown on the graph in Figure 26. While the computer calculation seems to follow the manual computations, there are points which differ significantly indicating that an error is sometimes introduced into the calculation by the computer. The last measure taken was to

cause another camera to capture images corresponding to different focus positions on the camera lens. The intensity of the image captured by the camera should be proportional to the inverse square of the f-stop. When integrated density measurements of these images were made, the same scatter was produced as shown in the graph contained in Figure 27. However, when only the mean density was measured, the results conformed to that expected from the relation of the lens opening to intensity (see Figure 28). Based on this finding, it appears that the problem in the integrated density calculation arises from the subtraction of the modal density from the mean density. The modal density is defined as the most frequently occurring pixel intensity within the area of interest after smoothing. It is a function, to some degree, of the size of the signal relative to the size of the area of interest. Nevertheless, a sound means of comparing the intensities of images was available in the mean density measurement.



(a)



(b)

Figure 25: Column Plot Average Comparison. The column plot average did not provide reasonable solutions when used as a quantitative measure of beam intensity. Measuring the area under the curve resulted in smaller areas being assigned higher values than greater areas. Figure (a) shows a curve whose area was computed to be larger than the curve in Figure (b).

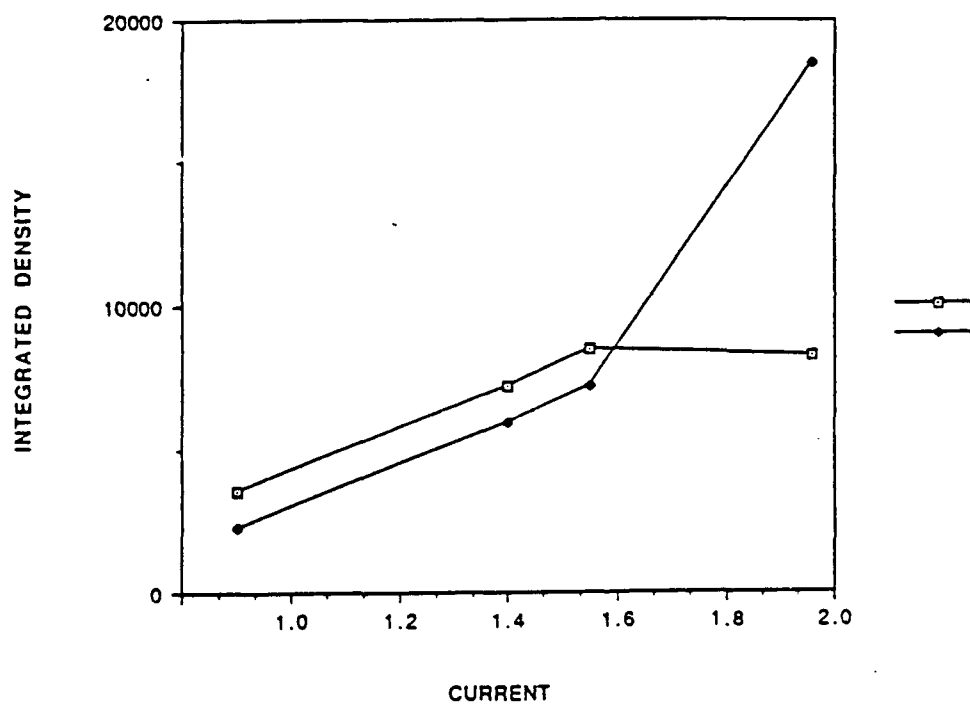


Figure 26: Integrated Density Study. The equation listed in the software manual to compute integrated density was used to manually calculate the integrated density. The results were compared and plotted against the computer calculation. The results show that the computer is not doing what it claims with significant deviation.

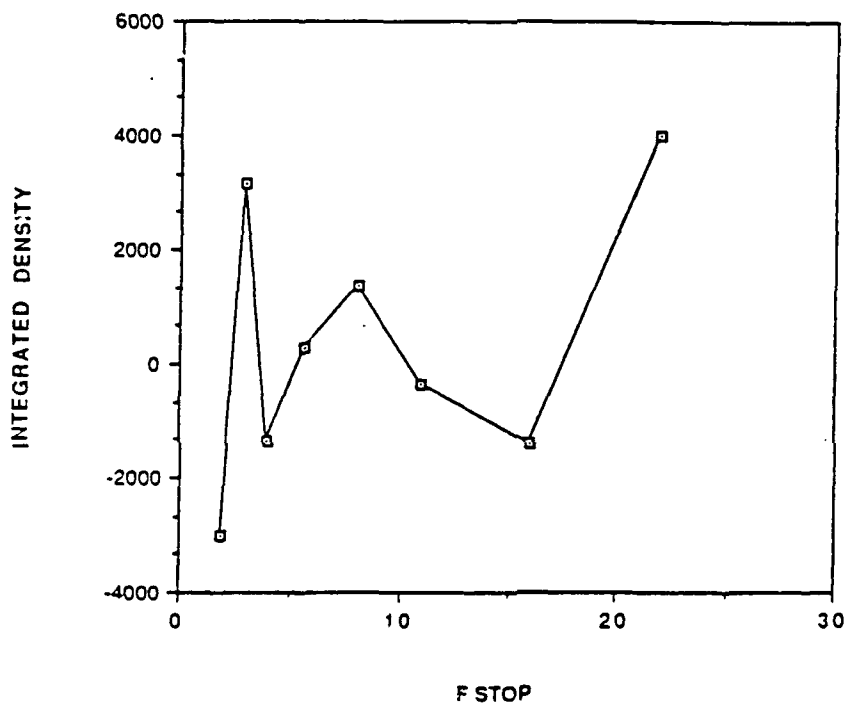


Figure 27: F-Stop Test. The camera was positioned to capture light images in a room of constant illumination. The camera lens aperture was positioned at each aperture opening (f stop). The image was captured and analyzed using the integrated density function. The image intensity should be proportional to the inverse square of the f stop. The results plotted above do not conform to this relation.

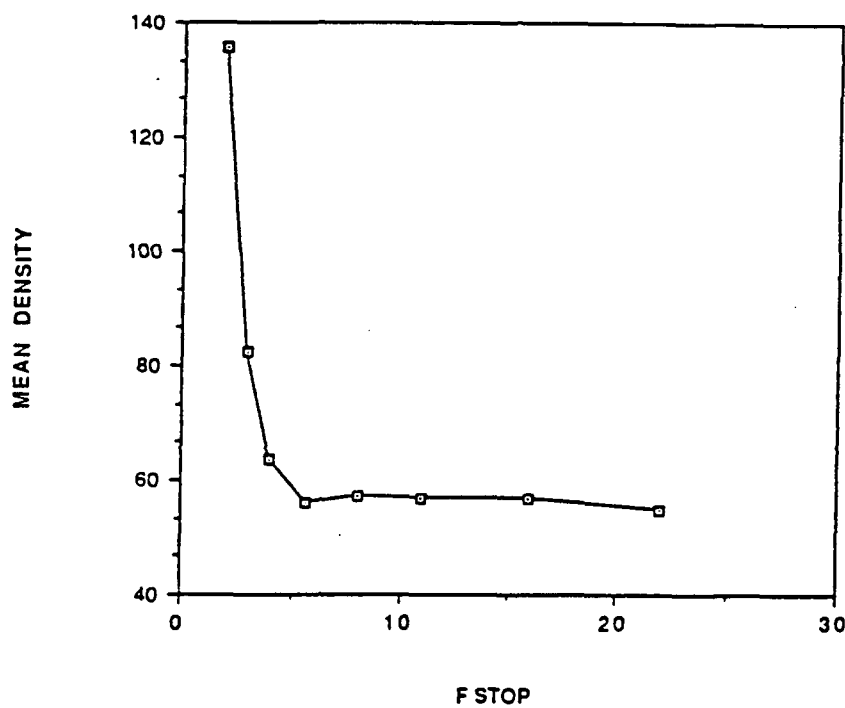


Figure 28: F-Stop Test. The same data in Figure 27 was analyzed using the mean density function. The results were in excellent agreement with the inverse square relationship of intensity with the aperture opening (f stop).

### C. DIFFUSE SCREEN EXPERIMENTAL PROCEDURE

The Beam Monitor experiment consisted of two smaller experiments. The first experiment compared the image intensity as a function of angle between a front surface mirror and the diffuse screen; the second compared the intensity of the beam profile or signal as a function of current between the diffuse screen and the fluorescent screen.

The experiment was begun by studying the effect of the angle on the image intensity. The front surface mirror was the first to be studied. The ladder was oriented at 45 degrees from the electron beam permitting the observation of backward OTR reflected 90 degrees from the electron beam and the bremsstrahlung radiation which continues forward with the electron beam. The 45 degree position was called the zero position for the purposes of this experiment. While oriented at zero, the first image was captured. The secondary emission monitor (SEM) current was 4.5 nanoamperes and held constant throughout measurements on the mirror. The SEM was calibrated during previous experiments and found to be 12 % efficient. The energy of the linac was recorded as 95 MeV throughout all measurements. The ladder was rotated to the left 213 steps or one degree. The image became barely visible at the -1.0 degree position. The next reading was taken after rotating the ladder back in the positive direction .5 degrees resulting in a absolute

position of -0.5 degrees (with counter clockwise being negative and clockwise being positive). The intensity improve significantly at this position. Another reading was taken at the zero degree position followed by one at 0.5 degrees to the right of zero. The image appeared similar to the one at -0.5 degrees. The next image captured was at 1.0 degrees. Again the intensity of the image dropped off dramatically. These measurements indicated that OTR from a mirror surface was observable from an angular range of less than 1.0 degree.

The same procedure was followed with the diffuse screen. Again the zero position was the ladder at 45 degrees from the electron beam. The beam could not be seen at an SEM current of 4.5 nanoamperes and was raised until the image was clear. The SEM recorded current was held steady at an SEM current of 20.0 nanoamperes. (This corresponds to 170 nanoamperes true current.) The first image captured was at the zero degree position followed by a large sweep to the right at 10 degrees. That reading was followed by a sweep in the opposite direction to the 5 degree position and again to the zero degree position. The direction of movement continued in the negative direction taking the ladder to -5 degrees and -10 degrees. At this position, the image was clearly weaker and an attempt was made to capture the beam profile at increments of 2.5 degrees starting at the -7.5



degree position. This was followed by images at the -2.5, 2.5, 7.5, 12.5 and 17.5 degree positions.

The next part of the experiment took relatively little time but produced interesting results. The comparison of the signal versus the current began with the diffuse screen at zero degrees. The SEM current was started at 5.0 nanoamperes and increased to 19.6 nanoamperes over five images. (True average current ranged between 42 and 170 nanoamperes.) This was followed with a similar comparison using the fluorescent screen. The beginning SEM current was 2.0 nanoamperes. A total of seven images were recorded ending with an SEM current of 4.05 nanoamperes. That concluded the data acquisition for this experiment.

For the second experiment, the end station was reconfigured to repeat the previous set of tests but with the emphasis on the shape of the profile as a function of the angle of the diffuse screen compared to the mirror and the florescent screen. The diffuse screen position was changed to 60726 on the ladder within the main scattering chamber. Several images were taken to verify the performance of the linac as well as the Pixelpipeline program using the Cohu camera. When the ladder was oriented at the zero degree position (45 degrees from the electron beam path), the OTR image from the front surface mirror was circular. As the ladder was rotated positively, the image grew narrow in the x direction and was elongated in the y

direction. The steering of the beam through the quadrupoles was recorded and the slits were closed to 200. The objective of this experiment was to capture images on the mirror, diffuse and fluorescent screens as a function of the angle. The procedure was fairly simple. The ladder was rotated and images captured for each screen by changing the ladder position prior to the next rotation. The images were integrated and captured using the Pixelpipeline software. The average time for integration was 30 seconds. Additionally, background images were captured corresponding to integration times and subtracted during the analysis phase of the experiment.

After capturing background images with the shutter closed in front of the camera, data was collected beginning at the zero degree ladder position. The SEM current was read at 3.00 nanoamperes and the energy was 90.56 MeV. The initial rotation was in the positive direction. Images were captured at increments of 0.5 degrees until the mirror no longer produced a signal large enough to analyze. This occurred at the 4.0 degree position. The next image was captured at five degrees. The angular increments were then increased to five degrees. This continued until the ladder was in the 35 degree position. At this position, the image changed drastically and was seen moving across the screen quickly with the rotation of the ladder to that point. The final (once the ladder had stopped rotating) image that was

visible on the screen was a well defined, focused circle indicating that the electron beam was now hitting the side of the ladder and not the diffuse screen. Realizing this, the ladder was rotated by increments of five, ten, 45 and eventually 225 degrees until the image was clearly seen on the diffuse screen again. The image was beginning to appear at the 345 degree position images captured at 350 degrees (-10 degrees from the zero position). The image, however, was still somewhat close to the noise level. The mirror surface did not produce a discernible image at all. After several images were captured on the diffuse screen without corresponding success on the mirror, the decision was made to restrict the search to the point at which the mirror produced a clearly visible OTR pattern on the mirror. At about the -3 degree position, the trace of OTR was beginning to appear. Subsequent images were captured reflecting more intense traces of OTR, but nowhere near the intensity level expected at these angles. Two possible explanations were considered. The first was that the linac was not producing an electron beam of sufficient current; and the second was that the controller had accumulated enough error in the rotation of the ladder so as to produce a false reading as to the actual orientation of the screens. After rotating through 360 degrees and beyond, the experiment was stopped. The end station was checked to see if the ladder was where the controller had indicated it

should be. This was done using the alignment laser used during the experimental set-up positioned on the opposite side of the scattering chamber from the Cohu. The laser indicated that the controller was not the source of the error and that the ladder was rotated well beyond the zero degree position. Having already produced excellent results at the beginning of the experiment within that range of angles, the linac had to be the source of the problem.

#### IV. PROFILE MONITOR DATA AND RESULTS

Analysis of the data acquired during the experiments suggests that the diffuse screen is an excellent beam profile capitalizing on the nature of optical transition radiation. The principle feature is its relative constancy in maintaining the beam shape to at least  $\pm 30.0$  degrees. The actual limits of the angular rotation could not be tested during these experiments due to the placement of the diffuse screen in the ladder. Based on the excellent intensity and profile shape of the image at the  $30.0$  degree rotation, there is every reason to believe that the actual limits are still greater out to around  $\pm 40$  degrees. The diffuse screen was also shown to increase the range over which the intensity of the OTR pattern is visible when maintaining a constant current. The diffuse screen was also less sensitive to fluctuations in the electron beam's performance. The mirror's tendency to saturate at higher currents at small angles required the decrease in current to obtain clear images. When the angles were increased, the current had to be significantly increased to capture images. The diffuse screen is also easily and inexpensively constructed and employed. Lastly, the diffuse screen does not produce secondary effects from the incident electron beam causing the OTR pattern to give a false representation

of the electron beam profile (as in the case of the fluorescent screen).

#### **A. ANGULAR DEPENDENCE**

The principal investigation of this experiment was the angular dependence of the OTR signal strength. The diffuse screen increased the range of observation to 27.5 degrees (Figure 30) during the first experiment; and it increased to  $\pm 30$  degrees (Figure 31) during the second using the integrate option of the Pixelpipeline software discussed in Chapter III. Previous OTR work stressed the change in shape of the OTR pattern as the ladder was rotated on the mirror. This limited the usefulness of the front surface mirror and similar materials for profiling the beam. If the diffuse surface of the aluminum screen increased the range over which the beam spot changed shape, it would be an inexpensive and simple means of profiling the beam during radiation experiments.

During preliminary analysis of the angular dependence of the mirror and the diffuse screen, it was clear that the diffuse screen increased the interval over which the ladder could be rotated while still maintaining the ability to profile the beam. The analysis was made by finding the peak intensity pixel location while oriented at the zero degree position. That was then selected as the vertical pixel height height of the scan. The scan was made from the same pixel location covering the same width for every

comparison. The profile plot option calculates the mean intensity for all pixels crossed during a horizontal scan. The mean intensity value was used as a crude but useful means of comparison. The result was that the mean intensity dropped within the range of -1.0 and +1.5 degrees on the front surface mirror. In contrast, the diffuse screen produced significant average intensities from -10 degrees to 17.5 degrees (see Figure 29). Though the last angle measured was 17.5 degrees, there was every indication that the range would continue beyond the 17.5 degree mark as the OTR image seemed clearer. These results came from the first experiment and raised an important question concerning methodology. The issue was whether the practice of changing directions to rotate the ladder introduced errors large enough to obscure the true angular readings. This was later addressed in the second experiment.

Recognizing that the best, most reliable tool in the Image 1.29 arsenal was the mean density function, the comparison was formally made comparing the mirror against the diffuse screen. The procedure taken was to first find the modal value of the images and subtract that value from all images corresponding to the vacuum/screen interface. The modal values proved to be the same for all images corresponding to surface type since the currents were held constant (within surface type). The graph in Figure 30 shows that the mean density dropped from as high as 18.78

to nearly zero (3.43 at -1.0 degrees) within the -1.0 to +1.5 range on the front surface mirror. In contrast, the diffuse mirror greatly extended the range of observation to at least 27.5 degrees from the 2.5 degree range for the mirror (see Figure 26).

The mean density function, when applied to data collected using the 'integrate' capability of Pixelpipeline increased the range of angles for both the mirror and the diffuse screen. Figures 31 and 32 show the positive and negative rotations. The positive rotation (Figure 31) shows that OTR intensity persists to at least 30 degrees for the diffuse screen while only to 4.0 degrees for the mirror. The negative rotation (though accuracy was limited by linac performance) supports the general trend established by the positive rotation. This suggests that the range of the angles of observation are as large on one side as on the other.



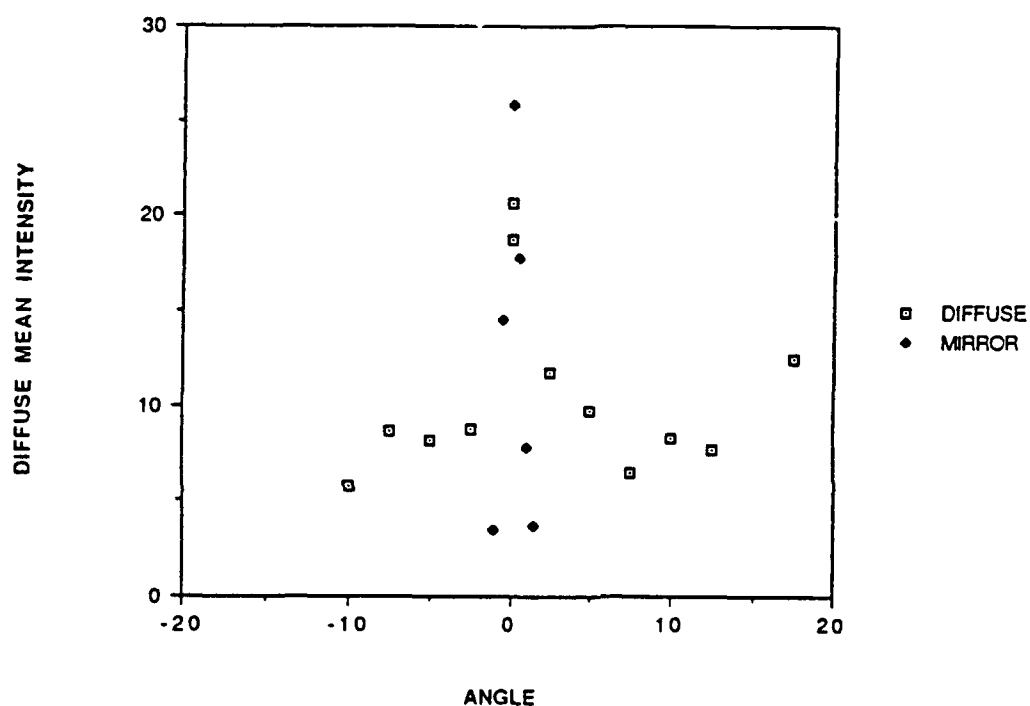


Figure 29: Signal Intensity versus Angle. The mean intensity of images captured on the front surface mirror are shown compared to those from the diffuse screen. The diffuse screen has a much wider range of angles over which the signal is detectable. Currents are held constant. Note that the mirror produces observable signals over an angular range of about 1.0 degree.

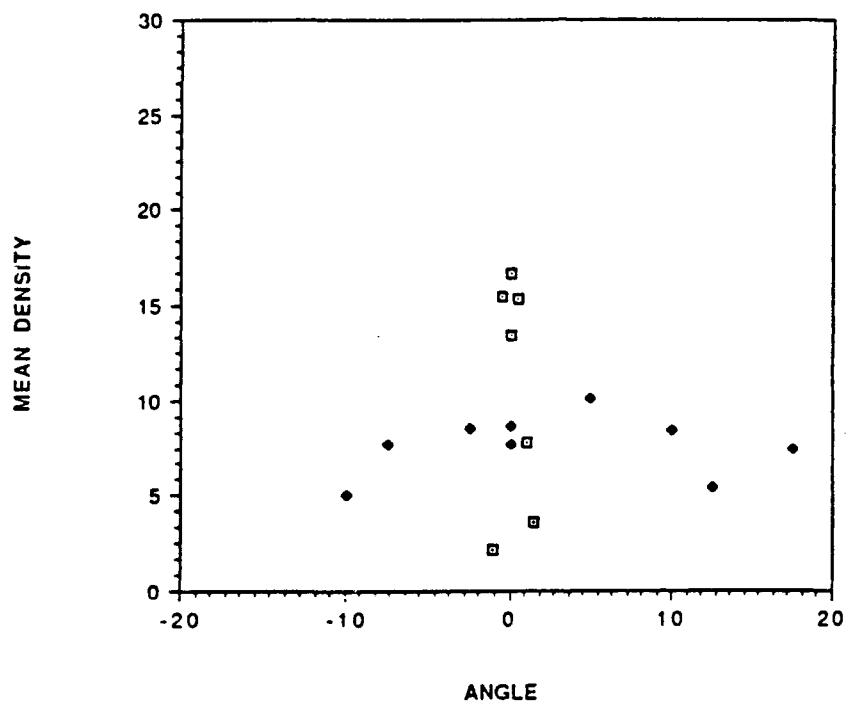


Figure 30: Angular Dependence. The mean density is plotted against angle showing that the diffuse screen preserves the OTR image well beyond the front surface mirror.

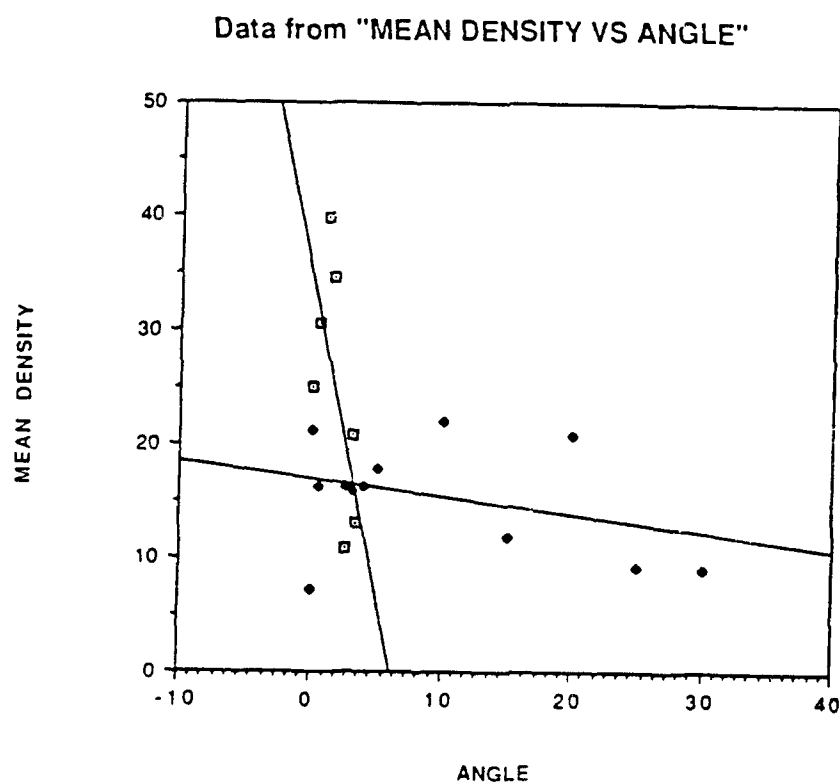


Figure 31: Mean Density vs Angle. The positive rotation is shown in this graph for the second experiment using the integrate option. The steep line is fit to the mirror values and the other line is fit to the diffuse screen values for mean density. The OTR from the diffuse screen is observable to 30.0 degrees.

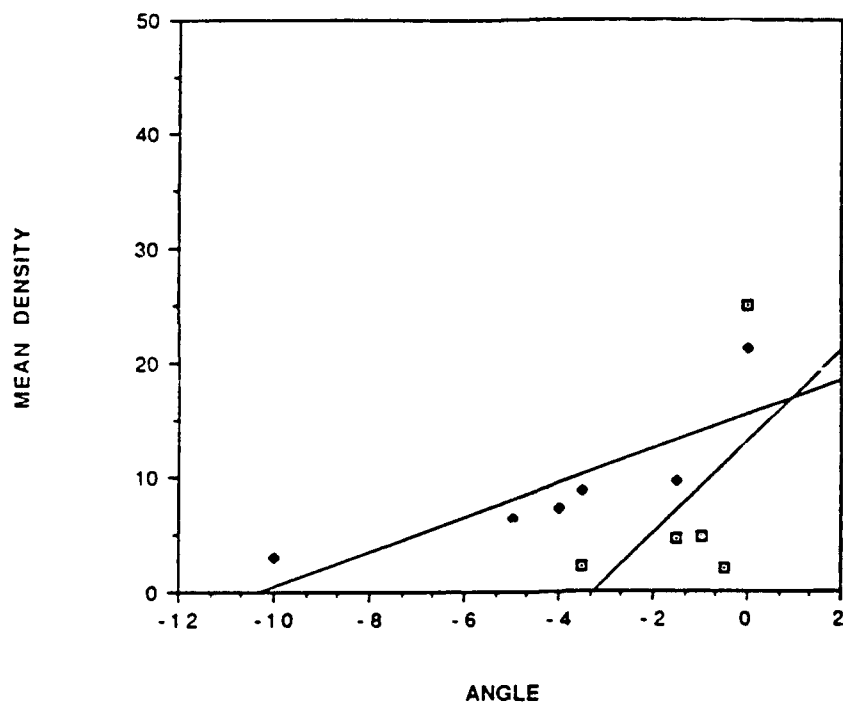


Figure 32: Mean Density vs Angle. The negative rotation is shown for the second experiment using the integrate option. The signal was limited by equipment problems. In spite of the equipment problems, there is a definite range extension with the diffuse screen over the mirror.

## B. CURRENT DEPENDENCE

This part of the experiment was designed to study the effects of current changes on the fluorescent screen and compare it to the performance of the diffuse screen. The electron beam incident on a fluorescent screen causing the atoms to spread outward radially from the beam center causes additional light production beyond the actual shape of the electron beam. Consequently, a corresponding increase of intensity was expected over the diffuse screen and mirror. Additionally, whether the shape of the curve is exponential or linear was of interest in studying the character of the fluorescent screen.

The images were again analyzed using the mean density function. The results showed the rise in intensity from an SEM current of 0.9 nanoamperes to an SEM current of 4.05 nanoamperes after which the image saturated. The impact of the size of the area of interest was investigated during the analysis. The first mean density measurement was made with an area 50 x 38 pixels. The results are plotted in Figure 34. The last two images were saturated at the higher currents and discarded. Nevertheless, the graph in Figure 33 clearly depicts an exponential growth in intensity with the current for the fluorescent screen. The diffuse screen data were analyzed in the same way as the fluorescent screen. A linear curve easily fit the data points from the mean density values (see Figure 34).

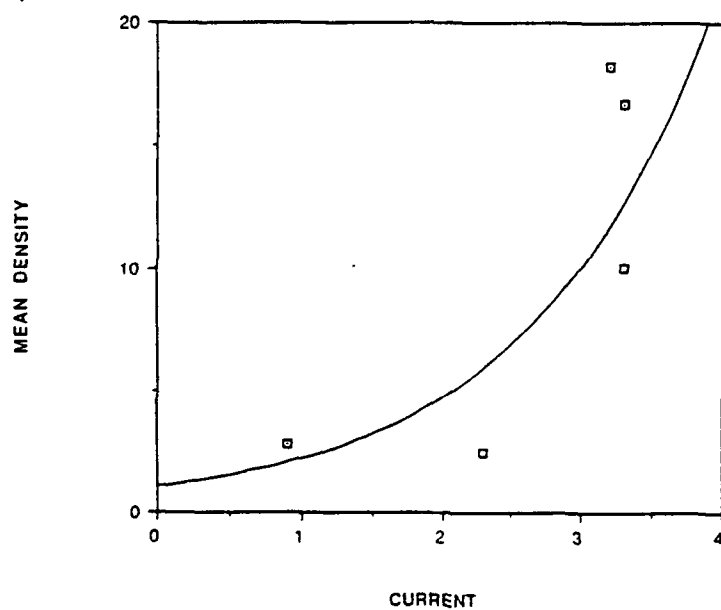


Figure 33: Current Dependence of Florescent Screen. The florescent screen mean density is measured against the current. As the current increases, the mean density increases exponentially.

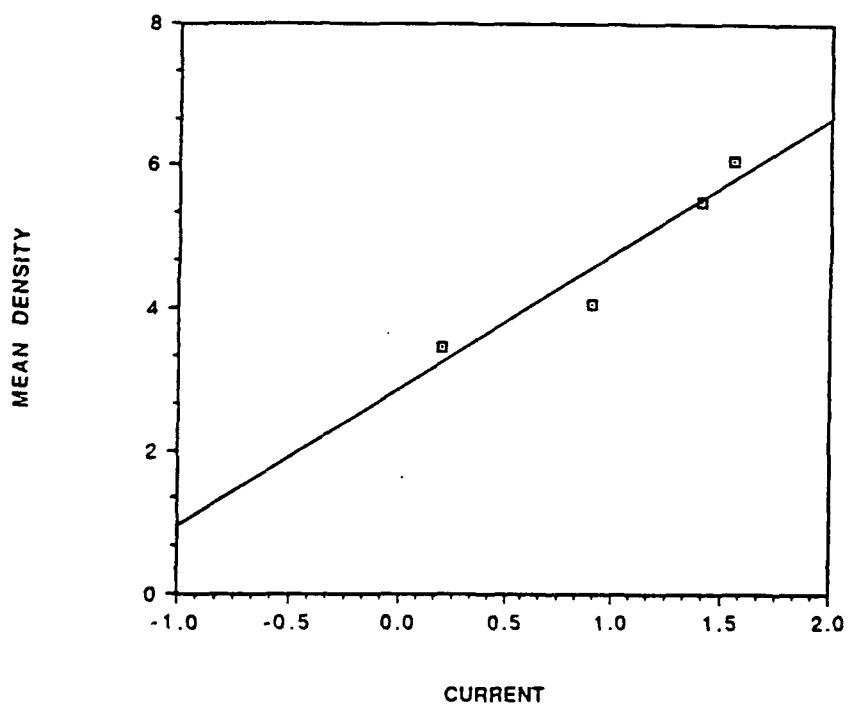


Figure 34: Current Dependence of Diffuse Screen. The mean density is measured as the current increases. A simple curve fit revealed a linear relationship. Further measurements should be made to verify linear relationship at higher currents.

## Profile Shape

The questions raised during the first experiment were investigated during the second experiment. The focus was on the shape of the beams OTR pattern to study the extent to which the diffuse screen preserved the electron beam's profile using the OTR pattern as a diagnostic. As mentioned during the procedure section, the variable of interest was the angular dependence. Current was adjusted when appropriate to produce a visible OTR image. The effect of backlash was controlled by rotating in one direction only. Comparisons between the OTR image produced by the mirror and those from the diffuse screen were made by changing the ladder height at the same angular position eliminating the introduction of error by making the measurements separately. The fluorescent screen was sampled at various angular positions to compare its shape to that of the diffuse screen as well.

The qualitative analysis of the profile was done using the profile plot and three dimensional plot options of Image 1.29. The profile plot was made by first determining the coordinates of the pixel of greatest intensity for the series of images beginning at the zero degree image. The y-coordinate of that pixel was 188. The x-coordinate to start the profile was selected as 186 providing a scan width of 119 pixels for all scans. The full width at the half maximum (FWHM) was measured to study the shape of each



profile. Figure 35 shows the graph of the FWHM of the gaussian profiles for the mirror. There are basically two levels of values depicted on the graph. The upper level are those produced during the initial sweep in the positive direction as shown in the graph contained in Figure 36. The downward direction of the FWHM is very clear until the intensity could not be separated from the background noise at positive four degree position. Upon continuing to rotate in the positive direction, faint traces of OTR were detected and measured at the -2 degree (358 degrees) position. The trend after returning to the zero degree position again is a slight increase in profile shape and is shown in Figure 37. As mentioned earlier, problems with the linac began to affect the experiment and obscured to some extent the true OTR pattern because the electron beam current could not be controlled. But some useful information is clear from the data. Figure 36 also shows the positive rotation covering the zero through four degree range over which the OTR pattern was visible. The slope of the curve fit to the data reveals a steady decline representing the deformation of the beam profile shape with the change in angle of specular reflection. Since the intensity of the OTR pattern was determined to be a strong function of the angle of specular reflection, the drop-off of intensity at the four degree mark is not surprising. The deformation to the profile shape, however, does not

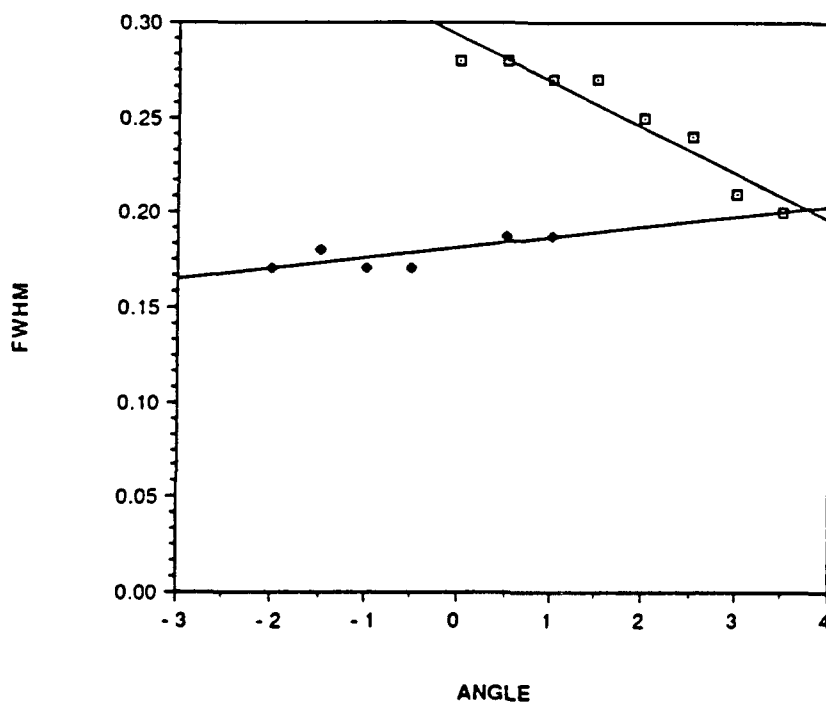


Figure 35: Mirror Profile Shape. The Full Width at Half Maximum (FWHM) was measured for line profiles taken at various angles. The graph shows the performance of the mirror and the decreasing FWHM away from zero degrees. The upper values reflect the positive rotation and a negative slope showing that the FWHM decreases as the angle increases. The bottom values show the FWHM decreasing on the opposite side of zero.

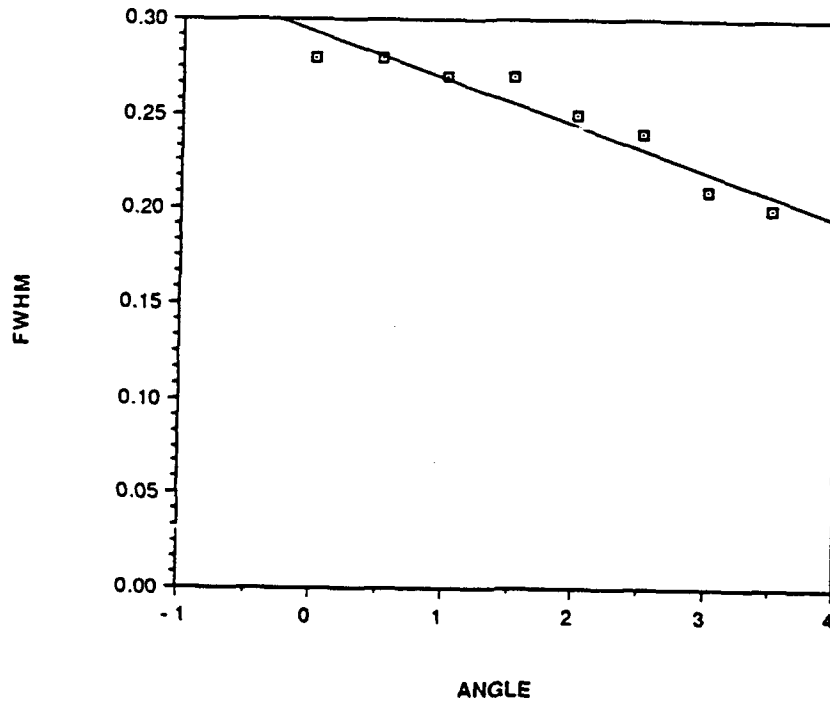


Figure 36: Curve Fit to Mirror FWHM. The slope of the line fit to the data from the front surface mirror is negative reflecting a decrease in the FWHM as a function of increasing angular displacement from zero.

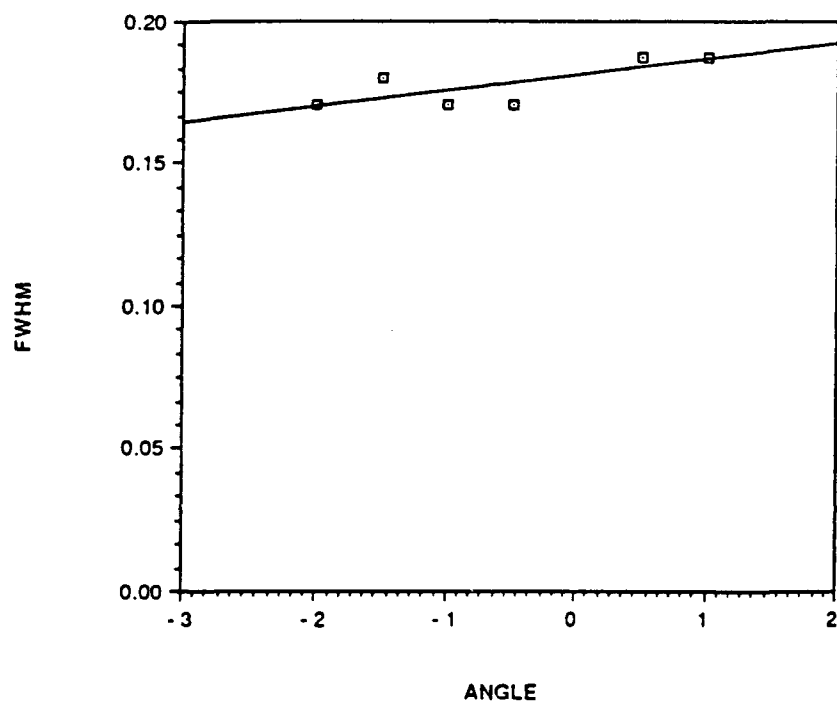


Figure 37: Mirror Profile Shape: The trend as the ladder traverses 360 degrees shows the FWHM increasing as the ladder returns to zero degrees.

drop off as quickly as illustrated by the slope of  $-8.30\text{E-}2$  intensity units per degree. But the trend is definitely smaller corresponding to the narrowing of the OTR image with an increase in angle. An important feature to note is that the OTR image intensity is proportional to the current and inversely proportional to the Lorentz factor. Consequently, the increased range of OTR intensity over the first experiment is consistent with the theory set forth by Ginsburg and Frank since the beam current was adjusted to higher levels to produce as many clear images as possible within the limitations of the NPS linac.

The diffuse screen results of the first experiment were reproduced nicely. However, this second experiment also sought to answer those additional questions raised during the first run. The extent of the increased range over the front surface mirror was investigated by rotating 360 degrees. As mentioned previously, the diffuse mirror continued to provide excellent OTR patterns until the edge of the ladder in which the screen was mounted prevented the electron beam from hitting the screen. This occurred at the positive 35 degree position as a function of the dimensions of the ladder frame with respect to the diffuse screen. The profiles were taken and measured in the same way as for the front surfaced mirror. Additionally, the problems with the linac had an impact on the diffuse screen, but to a lesser extent. Figure 38 shows the graph

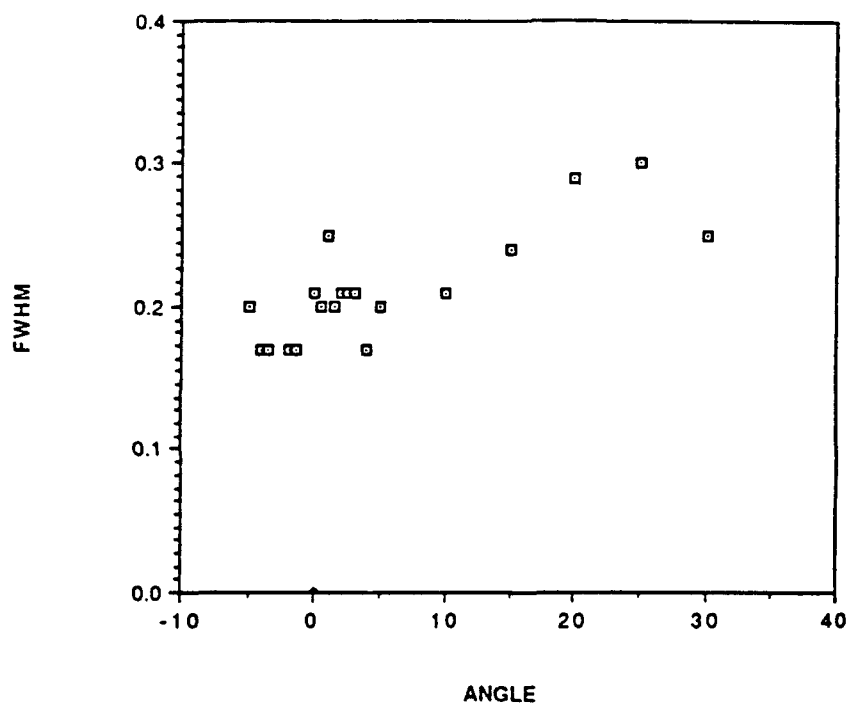


Figure 38: Diffuse Profile Shape. The FWHM from the line profiles were plotted as a function angle. The angular range is much wider than for the mirror.

of FWHM for the profiles created using the profile plot option. A quick comparison of this graph for the diffuse screen with Figure 35 for the front surfaced mirror shows much less scatter reflecting a more constant beam profile. A closer comparison shows that over the same range of angles (0-4 degrees) the diffuse screen produced nearly constant FWHM indicating a nearly constant profile. Figure 39 shows the straight line curve fit for the FWHM plotted against angle until the ladder frame obscured the screen. The slope of the curve is 0.0135 units per degree. The slope of the curve fit to the mirror data was six times greater in spite of the six fold increase in angular range over the mirror.

The positive slope suggests that the image width does not grow small with angle as in the case of the mirror.

The values acquired on the negative side of the rotation were recorded from -5 to -1.5 degrees. As previously stated, the linac began losing the ability to produce the quality beam experienced during the first part of the experiment. Nevertheless, the values for FWHM were nearly constant again (see figure 40). The change in value was attributed to the fluctuations in the linac. The slope of the curve is 0.017 units per degree which is less steep than the positive side of the rotation. Based on the preceding data, the diffuse screen preserves the beam profile shape with minor fluctuations. The mirror shape does not

deteriorate as fast as the intensity of the OTR image. But the shape deforms at a rate six to seven times faster than the diffuse screen.

Samples of the fluorescent screen showed a significantly wider FWHM than that found using the mirror or diffuse screen. Figure 43 shows the graph of the FWHM as a function of angle on the same scale as the mirror and diffuse graphs. This shows a definite increase in magnitude over the other surfaces as well as a slight, though clearly detectable increase in slope. Figure 41 shows the straight line fit to the data points giving a slope of 0.01 units per degree which is slightly less than the diffuse screen and eight and a half times smaller than the mirror. Thus, the shape of the curve generated by the profile plot option for the fluorescent screen changes least of all three surfaces. The positive slope indicates that the fluorescent screen generated image does not grow narrower with angle in agreement with the diffuse screen. The problem with using it as a beam profile stems from the previous discussion of the false profile that it presents. This is verified by the size of the FWHM relative to the mirror and the diffuse screen. The average FWHM for the fluorescent screen is 0.39 inches while the average for the diffuse screen and mirror are 0.23 and 0.24 inches, respectively. Combined with the practical problem associated with speed at which the surface



saturates with current, the fluorescent screens will not serve as a useful profile monitor.

### Three Dimensional Plot

The three dimensional (3D) plot gives additional qualitative information on the transition radiation produced by relativistic electrons. Figure 42 shows the OTR image of the shape of the electron beam incident on a front surface mirror. The image shows the electron beam has tails and is oval in shape, not circular. Figure 43 is the OTR image from the diffuse screen at the same angle of orientation (0.0 degrees). The diffuse screen and the mirror both reflect the same characteristic beam shape. The diffuse screen 3D plots of OTR support the previous findings. The 3D plots remain the same throughout rotation. Figures 44 and 45 show images taken at 5.0 and 20.0 degrees. The shape is nearly constant. The mirror, however, rapidly changed shape before reaching an angle of 4.0 degrees. At that position, OTR was not discernible from background noise.

Figures 46 and 47 are 3D plots of the fluorescent screen at 5.0 and 20.0 degrees, respectively. The strength of the fluorescent screen is its ability to preserve its shape independent of angle of observation. The fluorescent screen, however, does not provide an accurate representation of the electron beam profile or shape. It experiences secondary electron effects which distort the true image into a nearly circular pattern. Since the mirror at zero

degrees (Figure 42) profiles the true beam shape [Ref. 6], the difference in profiles (of the fluorescent and front surface mirror) suggests that the fluorescent screen, though independent of observation angle, does not accurately profile the true beam shape. This finding agrees with the FWHM study discussed previously.

This chapter has demonstrated that the diffuse screen is an excellent beam profile monitor. It expands the range of angles over which OTR can be seen, measured and analyzed. It is also less sensitive to electron beam fluctuations. Additionally, the OTR signal from the diffuse screen is a linear function of the beam current. These all combine to make the diffuse screen a useful beam diagnostic and monitor without the limitation of a single angle of specular reflection.

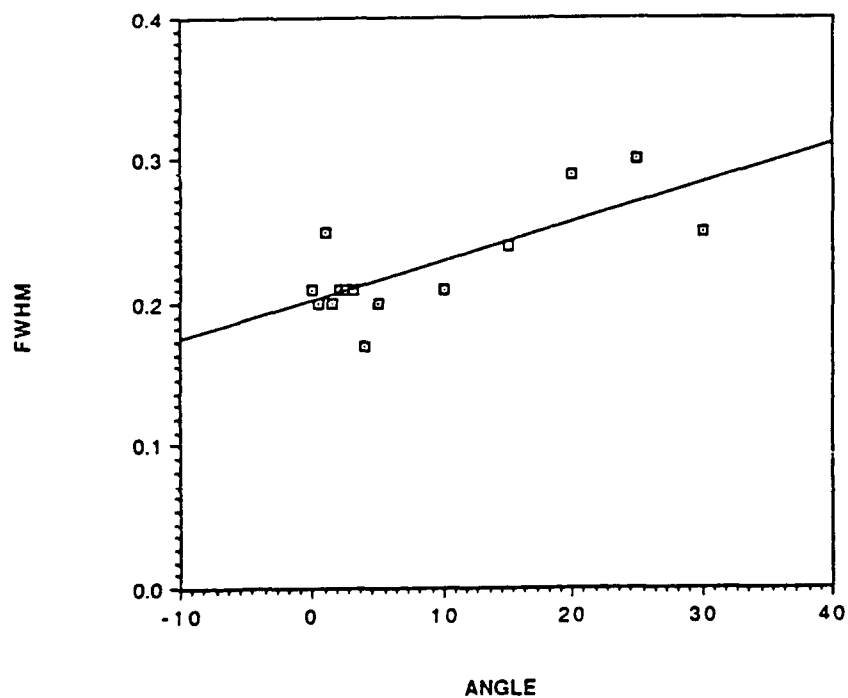


Figure 39: Diffuse Profile Shape. The slope of the line fit to the FWHM from zero to 30 degrees is non-negative and less than the slope for the mirror.

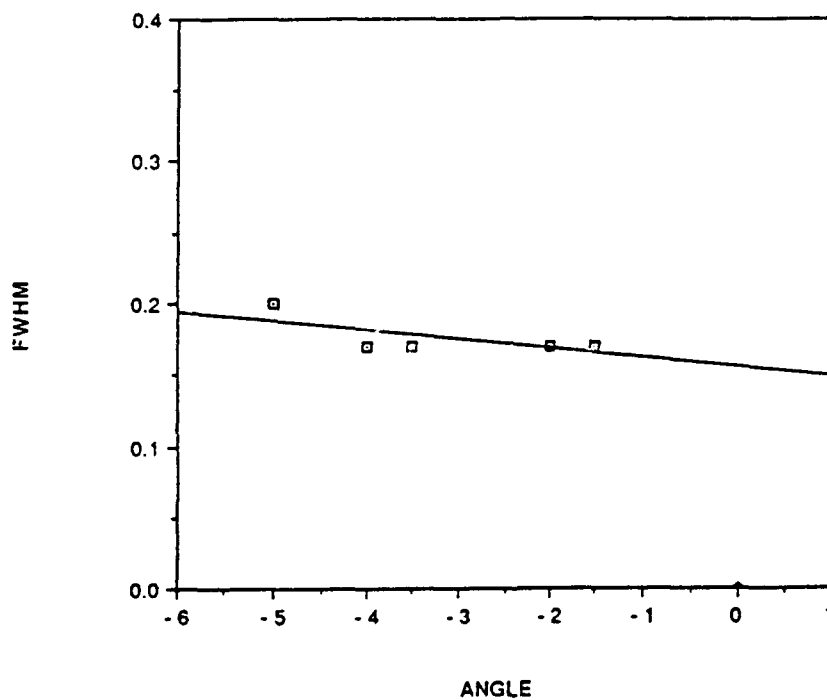


Figure 40: Diffuse Profile Shape. The slope of the line fit to the FWHM from 355 to zero degrees is also less than the mirror.

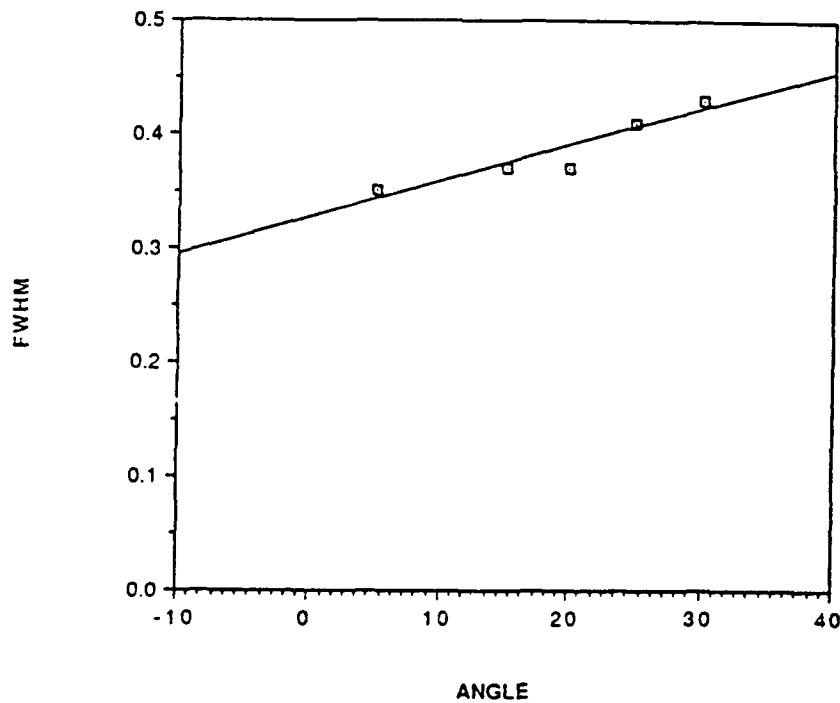


Figure 41: Florescent Profile Shape. The slope of the FWHM from the line profiles of the florescent screen with respect to angle is the smallest of all surfaces. The FWHM was most nearly constant.

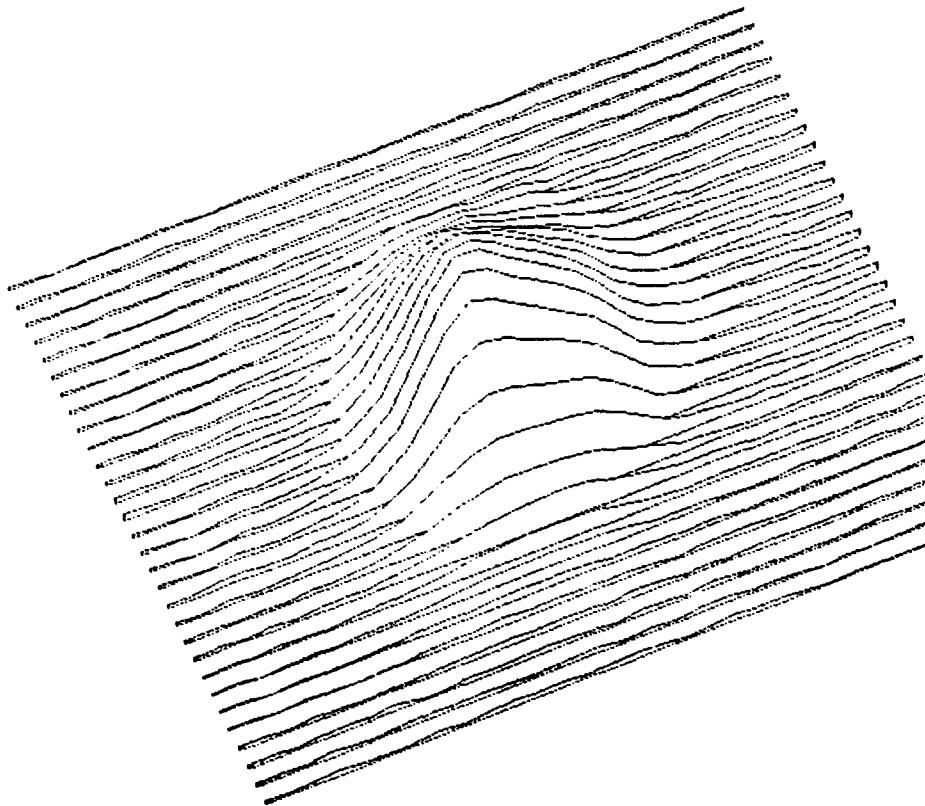


Figure 42: Mirror 3D Plot. The mirror is oriented at 0.0 degrees. The shape is oval and not circular.

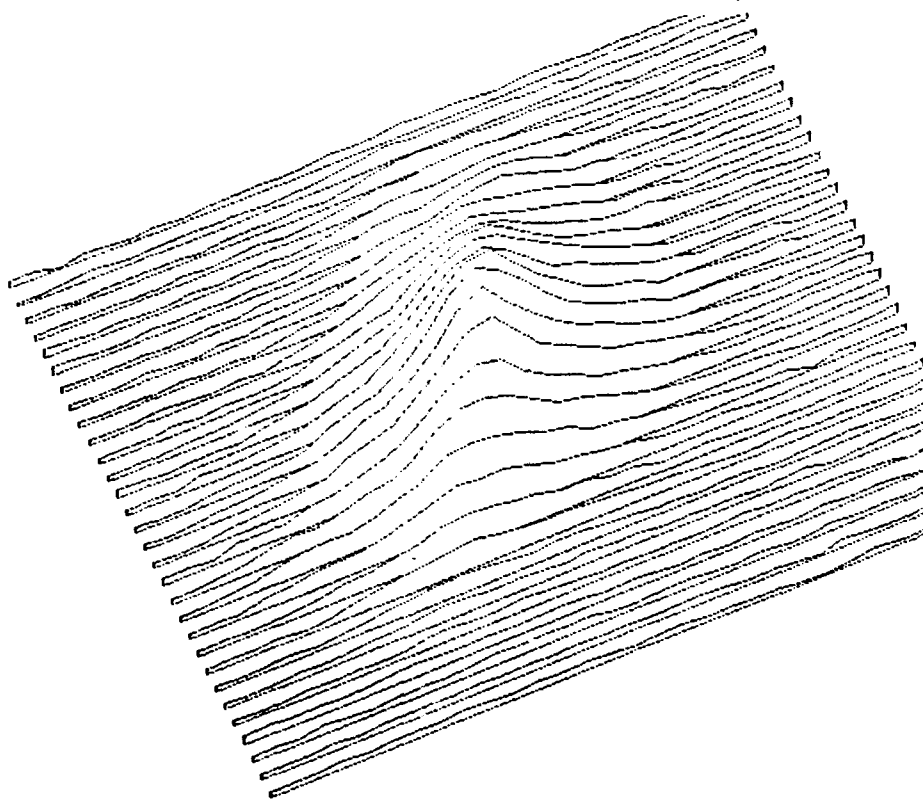


Figure 43: Diffuse 3D Plot. The screen is oriented at 0.0 degrees and retains the oval character of the mirror in Figure 42.

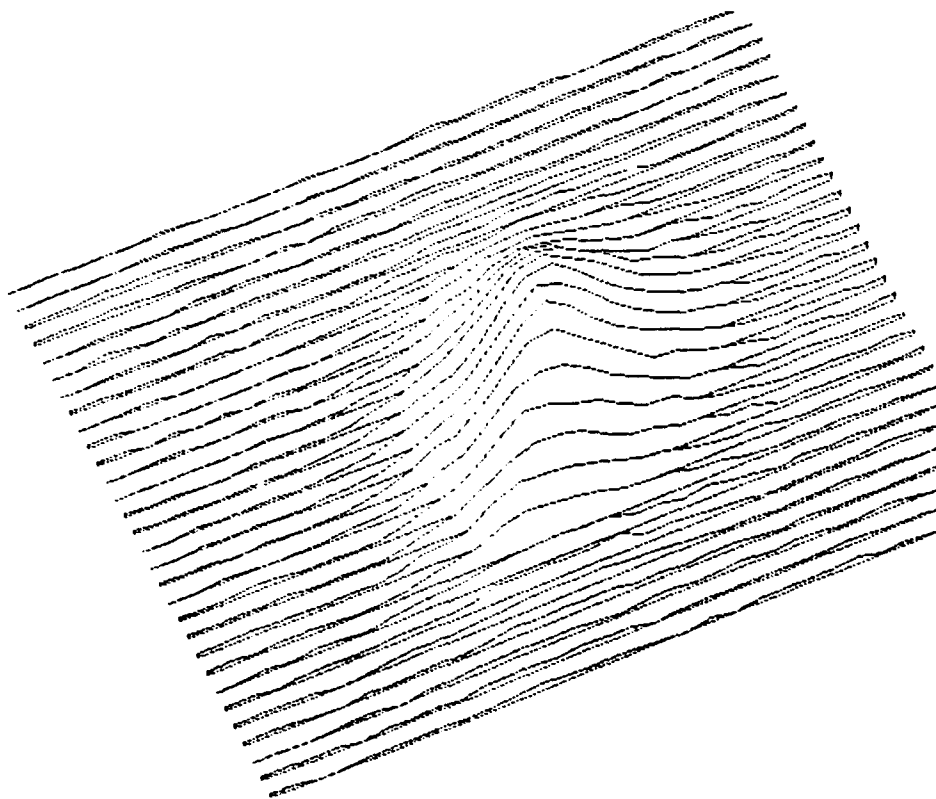


Figure 44: Diffuse 3D Plot. The screen is oriented at 5.0 degrees. The oval shape is retained.



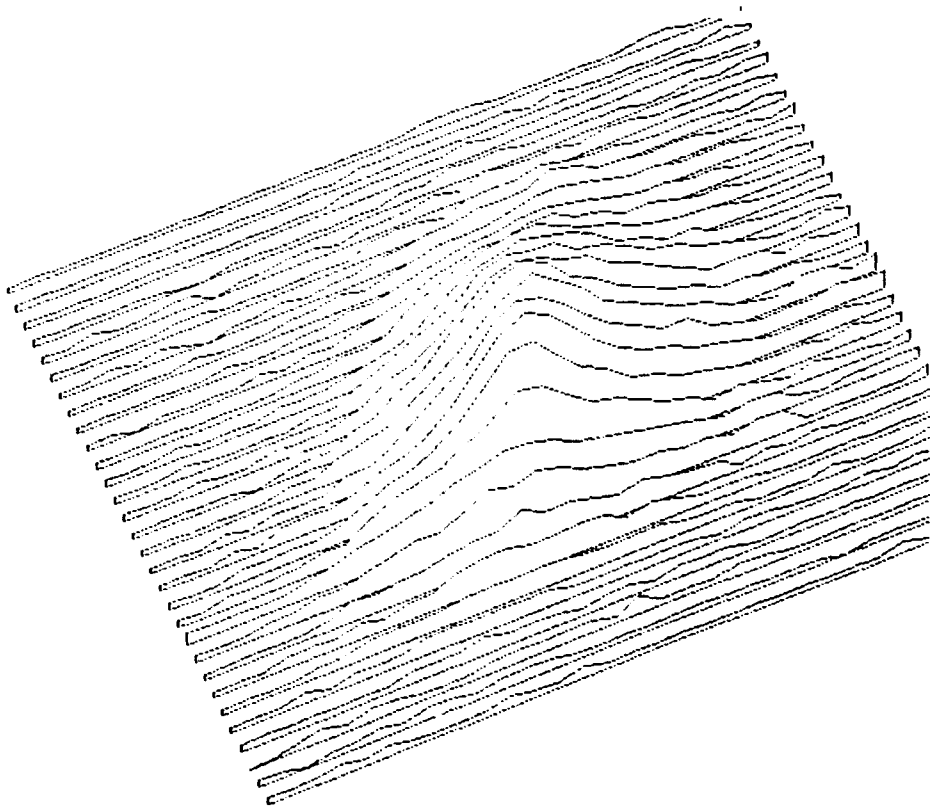


Figure 45: Diffuse 3D Plot. The diffuse is oriented at 20.0 degrees. The oval shape is preserved although the signal is closer to the noise.

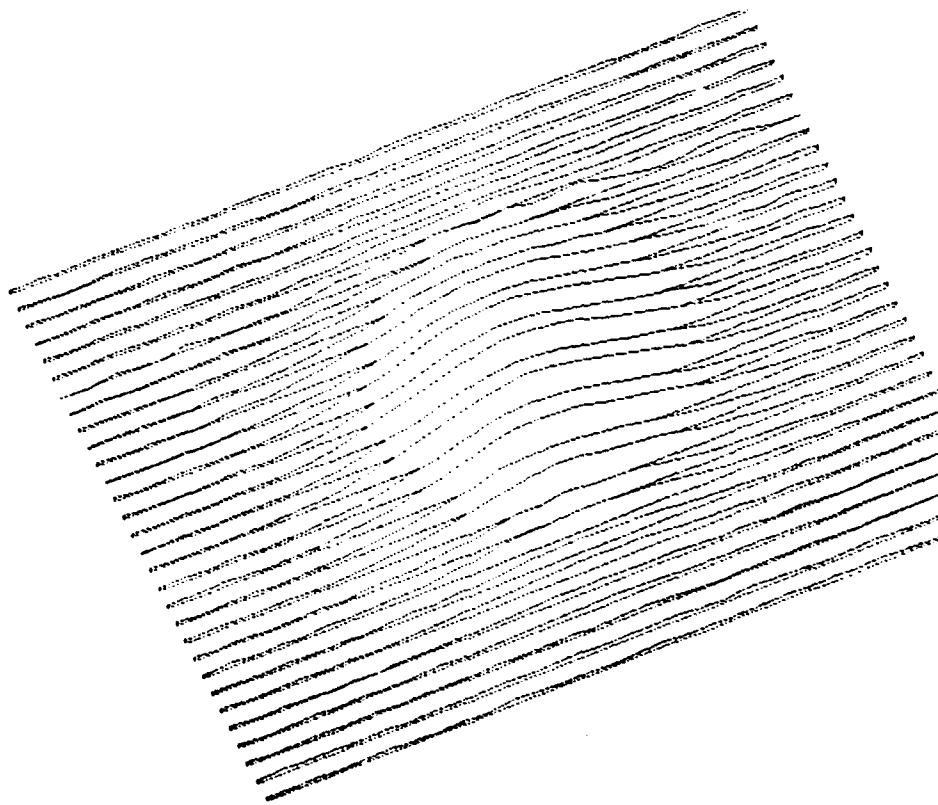


Figure 46: 3D Plot of Fluorescent Screen. The screen was oriented at 5.0 degrees. The image is more circular than both diffuse and the mirror shapes. The image is also wider.

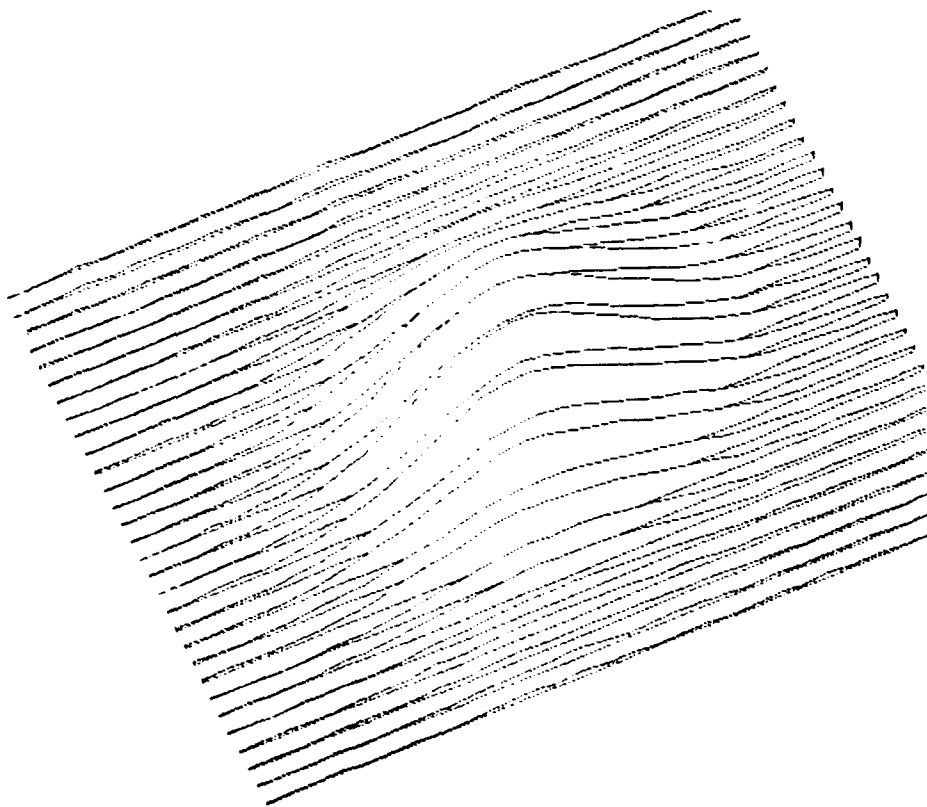


Figure 47: 3D Plot of Fluorescent Screen. The screen was oriented at 20 degrees. The signal is even wider and more circular than at 5.0 degrees. This screen preserves the FWHM better than the other two screens. But it preserves a false beam representation due to secondary electron effects.

## V. CONCLUSIONS

### A. EMITTANCE MEASUREMENT EXPERIMENT

The use of transition radiation as a beam diagnostic was demonstrated during the emittance measurement experiment. The OTR distribution pattern captured after the experimental setup revealed that the electron beam was not coincident with the laser beam used to align the optics. The laser was forced to follow path of the electron beam and the colinearity was confirmed using OTR. The remainder of the optics could then be aligned. The OTR was also used to identify peculiar behavior of the electron beam that might otherwise have gone unnoticed. Observation of beam displacement in the vertical direction was due to accelerator frequency change and was an example of the utility of the OTR as a beam diagnostic. The motion was caused by the misalignment of the linac sections and found to be frequency dependent. Oscillatory motion in the horizontal direction was found to be the result of an unstable, two component beam. Analysis of the OTR pattern led to the corrective action of reducing the width of the energy slits. Reducing the width of the energy slits also served to eliminate the distortion in the interference pattern due to the energy spread of the electron beam. Using OTR as an on-line beam diagnostic resulted in the

observation of a circular interference pattern suitable for emittance measurements. The data were obtained successfully and will be used to determine the NPS linac beam emittance.

#### **B. BEAM MONITOR EXPERIMENT**

The diffuse screen proved to be an excellent beam profile monitor. It accurately preserved the shape of the electron beam incident on the vacuum/metal interface to a range of  $\pm 30$  degrees. The intensity of the transition radiation produced by electrons was also found to be a linear function of the current measured by the secondary emission monitor (SEM). The diffuse screen is an inexpensive, easily constructed device which captures the actual beam profile and shape. For the purposes of this experiment, the diffuse screen was evaluated for angle and current dependence. It was compared to a front surface mirror and fluorescent screen producing convincing evidence of its efficacy as a profile monitor.

The diffuse screen demonstrated several advantages over the front surface mirror and the fluorescent screen. The principal advantage over the front surface mirror was its ability to preserve the electron beam profile over a wide range of angles. Rotation of the mirror quickly caused the visible OTR to be elongated and narrow. Thus, as the angular displacement increased, information about the electron beam was lost. The diffuse screen also accurately reflected the true shape of the electron beam. The

fluorescent screen preserved its shape over an equally large range of angular displacements. But the fluorescent screen's image did not accurately reflect the true beam shape. The secondary electron effects caused the image to be more circular than the electron beam and possess a much wider full width at half maximum. The fluorescent screen also demonstrated an exponential growth in its signal as the current was increased. Our results show that its signal increases linearly with the current. Future measurements to observe the linearity from the diffuse screen at higher currents is suggested.

The limitations of the Image 1.29 and Pixelpipeline software packages were also discussed. The Image software has a major flaw in the computation of Integrated Density designed to provide a quick area measurement of the signal intensity. The experiment demonstrated that the Mean Density was calculated properly and could be used in the interim as a quantitative means of comparison. The Column Plot Average function was also found to be lacking as a quantitative measure. Designed to calculate the area under the curve, the measure function provides highly inconsistent results indicating yet another problem with the software. The Pixelpipeline alone does not provide any analysis. The board and software were designed to operate with the Image software. The Pixelpipeline software, however, does permit more flexibility in data acquisition.

Unfortunately, the instructions are sketchy and require direct communication with the manufacturer to fill in omitted details. Lastly, in order to acquire integrated images while simultaneously performing background subtraction, the Applications Package must be ordered from Perceptics, the manufacturer.

### C. SUGGESTIONS FOR FOLLOW-ON RESEARCH

1. Study the linearity of the diffuse screen's signal with respect to higher currents.
2. Obtain the Perceptrix version of Image 1.29 for analysis.
3. Obtain the Perceptrix Applications Package to create simultaneous integration and background subtract.
4. Capture fluorescent screen images at zero degrees to compare with the mirror and diffuse. Be careful not to saturate. Seek ways to measure the SEM current at lower levels suitable for the fluorescent screen.
5. Reconfigure the ladder to permit a greater range of observation angles beyond 30.0 degrees.
6. Repeat measurements in Chapters 3 and 4 to refine data.

**APPENDIX  
EQUIPMENT LISTING**

PART NUMBER; NAME; FUNCTION

MANUFACTURER

Canon

200mm/1:2:8; Camera lens; focuses light pattern.

Newport Corporation

20Z20BD.1; 20th wave Zerodur ,irror, 2"; relfects light.

10Z20BD.1; 20th wave zerodur mirror, 1"; reflects light.

LS-35; 3' x 5' optical breadboard; for mounting components.

VPH-3; 3: rod holder; vertical post for mounting components.

VPH-4; 4: rod holder; vertical post for mounting components.

SP-3; 3: support post; form ounting components.

P-1, P-5; fixed height post; for mounting components.

MSP-1.5; 1,5" micro-support post; for mounting components.

MPH-2; 2" micro-post holder; hold micro post.

C-1; rod collar; maintains post height.

MPC; micro post collar; maintains post height.

MT-X; microtranslator stage; 1/4" travel stage.

MRL-3; micro optical rail; holds components to table.

MM-2; 2" square mirror mount; holds mirror.

LH2-T; simple lens holder; holds 2" diameter lens.

FH-2; filter holder; holds neutral density filters.

ID-1.0; iris diaphragm; aperture to control emitted light.

LM-2; lens mount; holds 2" diameter lens.

280; lab jack; large lab jack for 3" to 6" height control.

270; lab jack; smaller lab jack; 2: to 4: height control.

CL-4; tie-down clamp; all-purpose clamp.



CL-4; tie-down clamp; all-purpose clamp.  
360-90; angle bracket; sliding bracket for unusual mountings.  
B-1, B-2; sliding base; provides mounting base.  
BP-5; base plate; provides mounting base.  
400; dual-axis translation stage; 0.5" travel in 2 directions.  
481; rotary stage; for rotary motion.  
430-1; translation stage; 1" travel in one direction.  
CLMK-B2; lens holder; holds 2" diameter 200mm Canon lens.  
SP-6; support post; 6" long post for holding components.  
MB-2; magnetic base; magnetic holder for components.  
370; rod/clamp assembly; rod and clamp for holder laser.  
812; laser mount; two-axis control mount for laser.  
U-1301; laser; class IIIA, 1 milliwatt Helium-Neon laser.

Oriel Corporation

11512; large rail; 24" x 4" optical rail for mounting components.  
11522; standard rail; 24" x 2" optical rail, holds components.  
11601; large rail carrier; 5" square carrier mounts onto rail.  
11621; standard carrier; 3" x 3.5" carrier, mounts onto rail.  
11641; narrow carrier; 3.25" x 2" carrier, provides stable base.  
12055; tilt table; table tilts in horizontal plane in 2 axes.  
12312; standard rod; 2" long rod.  
12330; standard rod; 4" long rod.  
12350; standard rod; 6" long rod.  
14421; stable rod holder; 2" high rod holder.  
14432; stable rod holder; 4" high rod holder.  
14423; stable rod holder; 6" high rod holder.

12510; rod collar; for fixing rod height.

40780; plano-convex lens; 2" diamter lens, focal length of 100mm.

50350; neutral density filter, 1.0; reduces light to 10-%.

50360; neutral density filter, 2.0; reduces light to 1%.

27340; linear visible polarizer; 2" diameter, polarizes light.

14230; optical clamp; for holding optical components.

13872; 22: ridgid mount; legs for holding optical breadboard.

18011\*; Encoder Mike Controller; for controlling motorized stages.

13048\*; 360° motorized rotary stage; for precise rotary motion.

16338\*; 2" motorized translation stage; for precise linear motion.

18212-1-1200\*; electrical cord; connects motorized components with Encoder Mike Controller.

Ealing Electro-Optics, Inc.

2668P74; sector star target; for focusing light.

228437; electronic shutter; opens/closes to admit light.

228460; shutter mount; for holding shutter.

Process Physics, Inc.

C6C-0800\*; six-way vacuum chamber; holds OTR mirror.

HTE, Inc.

50054\*; standard 8" Conflat flange; for six-way chamber.

50360; nut, bolt, and washer set; 5/16-24 x 2 1/4.

50329; nut, bolt, and washer set; 5/15-24 x 1 3/4.

Duniway Stockroom Corp.

VP-800-600\*; glass viewport, 6" O.D., 8" flange O.D.; for viewing.

G-800; copper gaskets; 8" flange O.D. for coupling vacuum parts.

Cohu, Inc.

4815-5000; solid state, monochrome CCD camera; for viewing OTR.

Hamamatsu, Inc.

C1000\*; Silicon Intensified Target TV Camera and camera control unit; for view OTR.

C1440\*; frame memory image analysis system; digitizer for C100 camera.

\* signifies component (or equivalent) has been borrowed from Dr. F.B. Fiorito, Code R41, Naval Surface Warfare Center, Silver Spring, MD.

## REFERENCES

1. Frank, I. and Ginsburg, v. Radiation of a Uniformly Moving Electron Due to its Transition from One Medium into Another, Journal of Physics, Vol. IX, No. 5, pp. 353-362, 1945.
2. Naval Surface Weapons Report TR 84-134, The Use of Transition Radiation as a Diagnostic for Intense Beams, by Dr. D.W. Rile and Dr. R.B. Fiorito, pp. 3-12, Jul 84.
3. Invention Disclosure of Dr. D.W. Rule, et all for Transition Radiation Interference Spectrometer for Measuring Emittance and Energy and Divergence of Very Cold Charged Particle Beams, Navy Case No. 71, 490, pp. 2-5, Aug 88.
4. Maruyama, X.K., Fiorito, R.B., Rule, D.W., Iversen, S.G., Ladish, J.S., and Caldwell, S.E., Optical Transition Radiation Diagnostics or Low Emittance, High Energy, Charged Particle Beams, Proceedings of the IEEE Particle Accelerator Conference, pp. 575-575, Mar 87.
5. Wartski, L., Thin Films on Linac Beams as Non-Destructive Devices for Particle Beam Intensity, Profile, Centering, and Energy Monitors, Proceedings of the IEEE Nuclear Science Conference, Vol. NS-22, No. 3, pp. 1552-1556, Jun 75.
6. Dallman, P., Establishment of a Capability to Measure Optical Transition Radiation, Master's Thesis, Naval Postgraduate School, Monterey, CA., Dec 89.
7. Mitgarden, Calibration of the NPS Linac Energy Defining Slits, Master's Thesis, Naval Postgraduate School, Monterey, CA., p. 4, Sep 71.
8. Image 1.29 Software Instructions, National Institute of Health, Public Domain, pp., 22-26.
9. Pixelpipeline Software Instructions, Perceptics Pixeltools users Guide, pp. 4-1 - 4-14, May 90.
10. Caldwell, D.M., Observation and Analysis of Optical Transition Radiation at the NPS Linac and its Use for Diagnostics of Electron Beams, Master's Thesis, Naval Postgraduate School, Monterey, CA, Jun 90.

# INITIAL DISTRIBUTION LIST

Defense Technical Information Center Cameron Station Alexandria, VA 22304-6145	2
Library, Code 52 Naval Postgraduate School Monterey, California 93943-5002	2
Dr. K.E. Woehler, Code PH Department of Physics Naval Postgraduate School Monterey, California 93943-5000	1
Prof X.K. Maryuma, Code PH/Mx Department of Physics Naval Postgraduate School Monterey, California 93943-5000	1
Prof J.R. Neighbours, Code PH/Nb Department of Physics Naval Postgraduate School Monterey, California 93943-5000	1
Dr. R.B. Fiorito, Code R41 Naval Surface Warfare Center 10901 New Hampshire Ave Silver Spring, Maryland 20903-5000	1
Dr. D.W. Rule, Code R41 Naval Surface Warfare Center 10901 New Hampshire Ave Silver Spring, Maryland 20903-5000	1
Prof. Fred R. Buskirk, Code PH/Bs Department of Physics Naval Postgraduate School Monterey, California 93943-5000	1
Dr. T.I. Smith HEPL 13 685 Wildwood Lane Palo Alto, California 94303	1
Dr. D.W. Beck Department of Physics University of Illinois at Urbana-Champaign 110 W. Green St Urbana, Illinois 61801	1

Mr. D. Synder, Code PH/Ds  
Department of Physics  
Naval Postgraduate School  
Monterey, California 93943-5000

1

Mr. H. Rietdyk, code PH/Hr  
Department of Physics  
Naval Postgraduate School  
Monterey, California 93943-5000

1

CPT C.B. Reid  
Physics Department  
West Point, New York 10996

1